Title
Investigation of the Structural Features Controlling Kinetics and Thermodynamics of the Mercuric Ion Reductase Carboxy-terminal Tail

Author
Goodman, Russell Claire

Publication Date
2014

Peer reviewed|Thesis/dissertation

Investigation of the Structural Features Controlling Kinetics and Thermodynamics of the Mercuric Ion Reductase Carboxy-terminal Tail.

by

Russell C. Goodman

THESIS

Submitted in partial satisfaction of the requirements for the degree of

MASTER OF SCIENCE

in

Biophysics

in the

GRADUATE DIVISION

of the

UNIVERSITY OF CALIFORNIA, SAN FRANCISCO

ACKNOWLEDGMENTS

Susan M. Miller, for proposing a fantastically interesting project that involved a breadth of complex experimentation and keen chemical, structural and enzymatic insight. Also for providing financial support as aspects of the project were brought to conclusions and for extensive input into this manuscript.

John D. Gross, for providing direction and insight throughout the NMR portion of the work and helping develop my intuition for interpreting NMR spectra as they relate to protein dynamics.

Tanja Kortemme, for helping me understand the relevant conclusions that could be drawn from the results of the Rosetta work.

Jeff Mugridge, for teaching me the technical details of setting up and collecting data for simple NMR experiments.

UCSF Biophysics Graduate Program, for two years of funding.

and

Sara Green Goodman, for keeping my thoughts humble and consistently reminding me that happiness must be the primary force that directs our compass as we navigate through life's rather uncertain terrain.

Investigation of the Structural Features Controlling Kinetics and Thermodynamics of the Mercuric Ion Reductase Carboxy-terminal Tail.

by

Russell C. Goodman

Abstract

Mercuric Ion Reductase (MerA) is the primary protein in the mercury resistance *mer* operon for detoxifying mercury. Specifically, MerA is a disulfide oxidoreductase that uses FAD-mediated NADPH reduction of Hg(II) to elemental Hg(0), an innocuous form of mercury. This is accomplished through a 3-cysteine pair pathway, where the first pair on NmerA, a metallochaperone-like domain, scavenges Hg(II) from the environment, a second pair on the last 10 residues of the protein, denoted the C-terminal tail (CTT), moves the Hg(II) over a 15 Å distance from NmerA to a final cysteine pair in the catalytic core of the protein, where the 2-electron reduction of Hg(II) takes place. Given the ubiquitous nature of C-terminal tails in other oxidoreductases, such as theoredoxin reductase (TrxR), we endeavored to determine the residues that modulate the CTT *in* and *out* equilibrium that allows for efficient movement of Hg(II) through the MerA mercury pathway without being the rate limiting step of the enzyme. To elucidate these residues, we implemented the Rosetta FloppyTail protocol to gain insight into the residues that appeared to influence the stability of the CTT through polar and electrostatic interactions. This work resulted in determination of the ionic triad of residues: K99, E446, and K449. Steady-state and pre-equilibrium kinetics were used to determine the rates of Hg(II) acquisition by the CTT in mutants of

the ionic triad residues as an indirect probe of *in* and *out* conformation of tail. This was completed in conjunction with an attempt at identifying relevant residues to be used a probes in relaxation dispersion NMR techniques for obtaining information regarding the dynamics of the CTT of MerA. The results from these diverse techniques suggested that K99, E446, and K449 all play a role in modulating the tail dynamics, with K99 and K449 acting to constrain the tail to the dimer cleft and E446 acting to liberate the tail. None of our results oppose the notion that these residues also play a role in the chemical catalysis of the enzyme.

TABLE OF CONTENTS

INTRODUCTION

Overview

Mercury is a naturally occurring element of typically low abundance (Schroeder and Munthe, 1997); however, due to the increased use of mercury in our consumer products and burning of natural products containing mercury, such as coal and wood, we have effectively widened its distribution and release into the biosphere (Chakraborty et al., 2013; Ruiz and Daniell, 2009). Given the known toxicity of mercury to humans and other organisms, we will need to broaden our understanding of the known Hg(II) detoxification mechanisms to ensure we attain the resources required for cleaning Hg(II) polluted environments, such as by means of phytoremediation (Doucleff and Terry, 2002; Kramer, 2005; Salt et al., 1998).

Since the known mercury resistance pathway consists of a series of enzymes with both complex kinetic and dynamic properties, extensive biophysical characterization will need to be undertaken to fully understand how to apply these enzymes in an efficient manner to environmental cleanup applications.

Heavy Metal Requirements and Toxicity

Transition and heavy metals, such as lead, cadmium and mercury, have largely been considered to be toxic to human health. However, other metals, such as iron, copper and zinc, are essential to appropriate function of enzymes in various organisms, although they can be toxic when exposed in excess (Foster, 1983). Interestingly, in some cases, Pb, Cd and Hg can substitute for Zn in

enzymes, although they tend to induce altered specificity and function (Vallee and Ulmer, 1972). As a result, the line between toxic and essential metals is largely a function of exposure thresholds, as opposed to being a binary judgment.

In any case, heavy metals do frequently cause harm to human health. Arsenic is known to cause issues among various systems, including nervous, cardiovascular, respiratory, and gastrointestinal. Likewise, Pb, Cd and Mn can cause issues with kidneys, bones, and the nervous system (Inoue, 2013). It is believed that these diverse effects arise from the mechanism of heavy metal toxicity. In general, metals target biological defense mechanisms used for removing toxins from the body; therefore, prolonged exposure to certain metals ultimately induces excessive wear on cellular systems and tissues (Shukla and Singhal, 1984).

Given the toxicity of heavy metals and recognizing that heavy metals are used increasingly in industry, as fuel additives, and other consumer products, it is important to understand how heavy metals cycle throughout our environment to contaminate land and water in remote areas from their sources.

Cycling of Mercury in the Environment

Mercury, of all heavy metals, poses significant risks to the global community. In its elemental form, mercury is substantially more volatile, allowing for its ease of distribution in the atmosphere. Mercury can also be microbiologically transformed into highly toxic organic forms (e.g., methylmercury), causing mercury to incorporate and persist in the fatty tissues of

aquatic organisms, such as fish. As many animals use fish as a principle source of food, there results a significant bioamplification of mercury in the food chain. As a result, this requires a sound understanding of mercury movement within the environment so as to mitigate consumption of mercury contaminated organisms, and thus perpetuation of MeHg into various parts of the food web (Zahir, 2005).

The cycling of mercury in the environment is based on an oxidation/reduction cycle (Figure I1). Hg(0) exists as a gas in the atmosphere, which can freely distribute into various ecosystems until it is oxidized to Hg(II). Formation of Hg(II) from Hg(0) occurs by reaction with ozone or in water-saturated regions of the atmosphere, such as fog and clouds (Munthe, 1992; Munth and McElroy, 1992; Munthe et al., 1991). Precipitation works as the primary medium for transporting oxidized mercury species from the atmosphere and delivering it to the earth's surface, on both land and water (Mason et al., 1994).

The means by which mercury enters the biosphere is diverse. However, mercury release into the environmental cycle can be divided into two basic pathways: anthropogenic means and natural means. The former is largely from the burning of fuels and from industries that use Hg(II) as a catalyst in chemical reactions (Lindqivst et al., 1991). The natural release of mercury into the atmosphere is a result of natural disasters, such as volcanic eruptions and forest fires (Rasmussen, 1994). Natural sources also include volatilization of elemental mercury from water or land (Nriagu, 1989; Gustin et al., 2008). The contribution of natural and anthropogenic mercury release into the environment is about equal;

however, the anthropogenic contribution has decreased over the last 30 years (Mason et al., 1994; Lamborg et al., 2002; Gray and Hines, 2006).

While developed countries have largely decreased their contribution of mercury emissions, developing countries (e.g., Asia and South America) are still contributing a large amount of mercury into the global cycle. In fact, Asia alone contributes 65% of the worldwide anthropogenic mercury (AMP/UNEP, 2008; UNEP Chemicals Branch, 2008). This indicates that mercury exposure will continue to be an issue we must contend with on the global scale, which necessitates a deeper appreciation for work investigating the molecular mechanism of mercury toxicity and cellular defense systems.

Hg(II) Toxicity

The concern regarding the deposition of mercury on land and in waters is a reflection of the toxicity of inorganic and organomercurial compounds. This toxicity derives from the high affinity of Hg(II) for cellular thiols, having a $K_{formation}$ for -S--Hg--S- of 10^{40} M^{-2} (Cheesman et al., 1988; Vallee and Ulmer, 1972). Thiols are present in important metabolites, such as glutathione (GSH), and in proteins as structural or catalytic components in almost all organisms (Clarkson and Magos, 2006). When mercury binds to these thiols, it effectively abrogates their function, rendering GSH inaccessible and proteins ineffective.

Inorganic mercury tends to be considered less toxic than organomercurial compounds (Harada, 1995). This derives from the favorability of hydrophobic compounds to diffuse through and incorporate into cellular membranes and

organelles and the fatty tissues of organisms. Perhaps the most publically recognized dangers of organomercurials was the Minamata, Japan MeHg exposure, where a local factory had used mercury as a catalyst in the production of acetaldehyde. The release of mercury from the industry contaminated the local bay, which ultimately caused the accumulation of MeHg(I) in fish. The consumption of the fish resulted in many neurological issues, and in some cases led to brain damage or death, in the people of the Minamata community (Lindqvist, 1991).

It is evident why public awareness of the toxicological effects of mercury has resulted in significant concerns regarding exposure to mercury through consumption of organisms with substantial accumulated mercury in fatty tissues. In fact, many articles have been published regarding the concerns of mercury exposure from diverse sources, such as mining to pharmaceuticals (Kang-Yum and Oransky, 1992; Hilson et al., 2007). Fortunately, there exist natural mechanism for reducing Hg(II) to the less toxic elemental mercury (i.e., Hg(0)), which have been used for cleaning mercury contaminated areas (Doucleff and Terry, 2002; Kramer, 2005; Salt et al., 1998).

Cellular Defense Mechanisms

Facultative bacteria and archaea possess the *mer* operon, which contains an assortment of genes necessary for the efficient processing of cellular and exogenous Hg(II) and organomercurials (Barkay, 2003). A subset of these

proteins is depicted in Figure I2 and consists of MerR, MerP, MerT, MerB, and MerA.

MerR is the regulatory component of the *mer* operons, which are often associated with transposable elements, such as Tn*21* and Tn*501* (Brown et al., 1983; Brown et al., 1984; Brown et al., 1986; Barrineau et al., 1984; Barrineau et al., 1985). Structurally, MerR is a homodimer that activates *mer* genes in the presence of, and a repressor in the absence of, Hg(II) salts (Lund et al., 1986; Lund and Brown, 1989). The MerR family of regulators posses interesting characteristics that allow the conserved N-terminal DNA binding region to alter the promoter region of the DNA in the absence of Hg(II) (Heltzel et al., 1990; Ansar et al., 1995), which prevents RNA polymerase binding, however, forms a binding site for RNA polymerase on the MerR protein to keep it nearby in the case of mercury exposure (Kulkarni and Summers, 1999; Ansari et al., 1991). Binding of Hg(II) in a 3-coordinate tri-cysteine complex at the ends of an antiparallel coiled-coil allosterically induces changes in MerR (Zeng et al., 1998), which allows for the restoration of the promoter DNA, and subsequent binding of RNA polymerase (Kulkarni and Summers, 1999; Ansari et al., 1991). Many of the MerR details have been discussed elsewhere (Brown et al., 2003)

MerP is a periplasmic monomer consisting of 72 residues (Jackson and Summers, 1982). It binds exogenous Hg(II) via a linear 2-coordinate complex formed from two MerP cysteine residues (Steele and Opella, 1997). MerP works in conjunction with MerT to ensure sequestered Hg(II) in the periplasm of the cell is delivered to the cytosol (Hamlett et al., 1992; Lund and Brown 1987).

MerT is a transmembrane protein consisting of 116 residues. Although there is no known structure of MerT, bioinformatics work has predicted that it contains three helices that transverse the membrane (Wilson et al, 2000). The transmembrane helices contain two cysteine pairs, a pair on the periplasmic side and a pair on cytosolic side (Sahlman et al., 1997). The periplasmic cysteines obtain Hg(II) from MerP, and the cytosolic cysteines are believed to pass Hg(II) to NmerA (Barkay 2003).

Charged species, such as some Hg(II) salts, need to be transported into the cell via the discussed sequestration and transport mechanisms. However, organomercurials – those possessing C-Hg bonds – can easily diffuse through the membrane and enter the cell (Hong et al., 2010). For processing these species, the *mer* operon also evolved an additional protein referred to as MerB (Furukawa and Tonomura, 1971). MerB is relatively small at 22.4 kDa (Begley et al., 1986). It works by means of a protonolytic cleavage (Begley et al., 1986). Initially, two catalytic cysteine residues coordinate the organo-mercury complex and cleavage occurs by way of a catalytic proton from a nearby aspartate residue (Lafrance-Vanesse et al JBC 2009, Parks et al JACS 2009). Following cleavage of the organic component, the two catalytic cysteines coordinate the Hg(II) in a 2-coordinate complex (Barkay et al., 2003). The action of MerB on organomercurials produces the organic species and the cationic Hg(II) species, where the latter is subsequently sequestered and reduced by mercuric ion reductase (MerA).

MerA is a disulfide oxidoreductase. Its primary function is to sequester and reduce Hg(II) to Hg(0), a volatile and innocuous form of mercury (Engst and Miller, 1999). As suggested, MerA plays a critical role in the *mer* operon Hg(II)-detoxification pathway. While most other Mer proteins are involved with mere sequestration or transport of Hg(II), MerA reduces Hg(II) to Hg(0), an innocuous form of mercury, which necessitates intricate biophysical characterization of MerA to fully understand its capabilities for applications in environmental health.

Mercuric Ion Reductase: Structure and Function

MerA has been studied extensively since the Tn*501*-encoded form was first purified in the early 1980s (Fox and Walsh, 1982). Structurally, MerA is a homodimer with each monomer consisting of an approximately 70-residue N-terminal domain (NmerA) connected to the nearly 500-residue catalytic core by a 30-residue linker (Figure I3a) (Brown et al., 1983). On the subdomain level, the core contains a flexible 10-residue C-terminal tail (CTT) (Schiering et al., 1991) near the binding site of NmerA and the pathway for mercury transfer. There are pairs of cysteine residues on NmerA, the CTT, and in the catalytic core, all of which are used for efficient transport or catalytic activity of MerA (Figure I3b), although it has been shown that the NmerA cysteines are not required for turnover of simple Hg(II) salts (Fox and Walsh, 1982; Moore and Walsh, 1989). Finally, MerA contains a binding site for NADPH near a bound FAD prosthetic group (Figure I3c) (Furukawa and Tonomura, 1972).

Functionally, NmerA scavenges Hg(II) from proteins in the cellular milieu (Ledwidge et al., 2005). Depending on the orientation of NmerA, the CTT may move within or extend from the dimer cleft and obtain the Hg(II) from NmerA. The flexibility of the CTT allows efficient delivery of Hg(II) to the catalytic cysteine residues in the core where Hg(II) is reduced to Hg(0) via a 2-electron transfer from NADPH, which is mediated by the bound prosthetic group FAD (Fox and Walsh, 1982; Ledwidge et al., 2005).

Of particular importance in the functionality of MerA is the regulation of the flexibility of the CTT to populate both an *out* and *in* state, where retrieval of Hg(II) from NmerA and delivery of Hg(II) to the catalytic core can occur, respectively, yet still maintain sufficiently high rates of transfer as to not limit the rate of the reaction. In wild-type MerA, the rate limiting steps of the reaction involve the reduction of Hg(II) while bound to the inner cysteine pair and dissociation of NADP+ (Engst & Miller, 98,99; Sahlman et al 1984).

Rates and States in Enzyme Catalysis

The interplay between protein dynamics and enzyme catalysis has become an increasingly studied subject (Nashine et al., 2010). Kramers in 1940 suggested that intrinsic dynamic fluctuations away from the ground-state enzyme-substrate complex led to the transition state and conversion of substrate to product. Nearly sixty years later in the early 2000s, work on cyclophilin A (CypA) (Eisenmesser et al., 2005) partially corroborated this notion by using NMR relaxation techniques to minimally reveal that the rate of turnover of CypA correlated with

the intrinsic dynamics of the enzyme, which was significant since it revealed that protein dynamics play a significant role in enzyme kinetics, yet not necessarily chemical kinetics.

Similarly, the dynamics of the MerA CTT are predicted to be a significant component dictating the overall feasible rate of Hg(II) turnover. It is interesting to note that MerA represents only one protein of many oxidoreductases that utilize a dynamic CTT of approximately 10-20 residues to deliver electrons or substrates to or from the active site for later reduction events. Some of these proteins consist of thioredoxin reductase (TrxR), a TrxR/glutaredoxin fusion (TGR), and ribonucleotide reductase (RNR) (Fritz-Wolf et al., 2007; Huang et al., 2011; Zhang et al., 2013). This suggests that understanding the interplay between the dynamics and kinetics of the CTT in Hg(II) acquisition with MerA will be significant in elucidating what appears to be a general protein biophysical mechanism.

Some work has already been completed in other systems to determine the parameters that dictate CTT flexibility. Fritz-Wolf et al. in 2007 investigated states populated by the TrxR CTT, finding a three-state model where the guiding bar residues – W407, N418, and N419 – all stabilized the CTT. Given the similarity in function between the CTT of TrxR and MerA, we suspect a similar set of residues must exist in MerA, which regulate the states and rates of the CTT of MerA. We believe that elucidating these residues is critical to gaining a complete understanding of the MerA kinetic pathway.

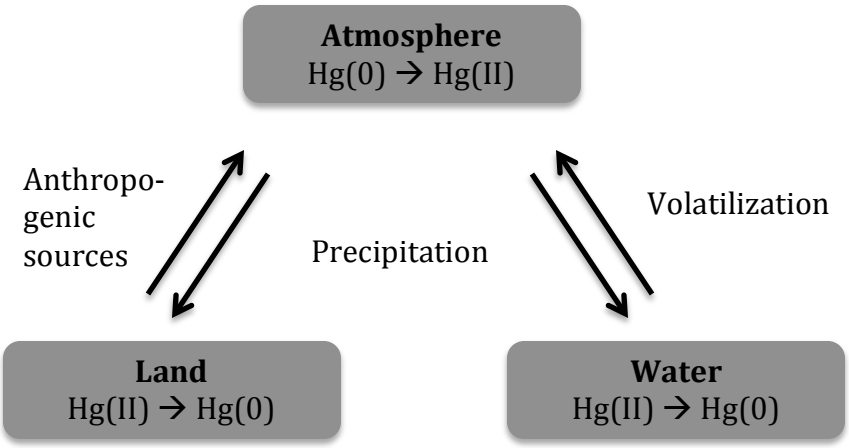

Figure I1. The mercury cycle. Movement of mercury between the atmosphere, land, and water occurs by means of an oxidation/reduction cycle, where soluble oxidized Hg(II) is carried to the earth by precipitation and reduced back to volatile elemental mercury.

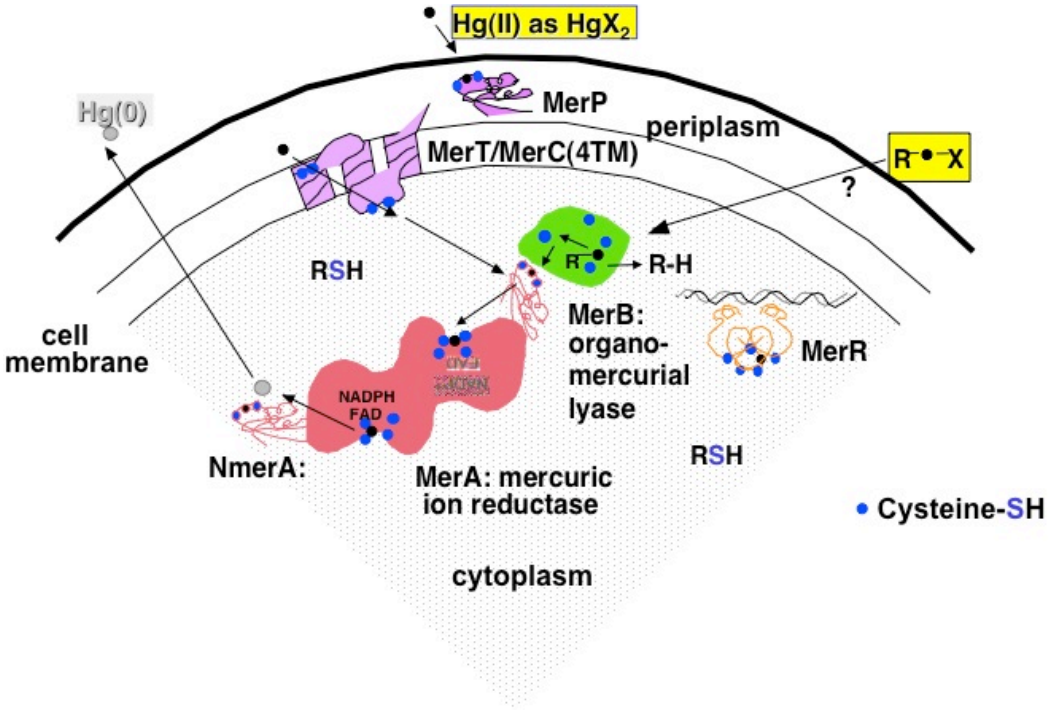

Figure I2. Overview of cellular *mer* operon proteins. Arrows indicate the flow of mercury into the cell as mercury salts (e.g., $HgCl_2$, $Hg(SG)_2$) or organomercurials (e.g., MeHg) and out as elemental Hg(0). The *mer* operon proteins sequester, transport and process the mercury compounds to diffuse out of the cell as elemental mercury.

(a)

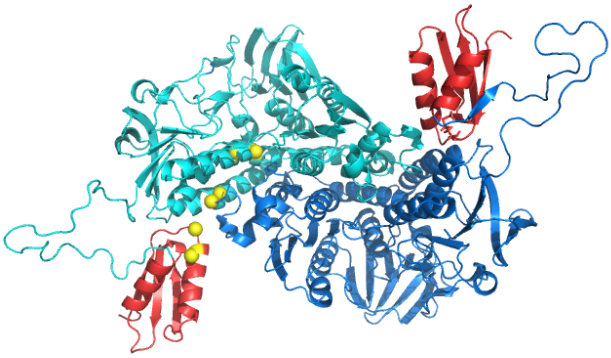

(b)

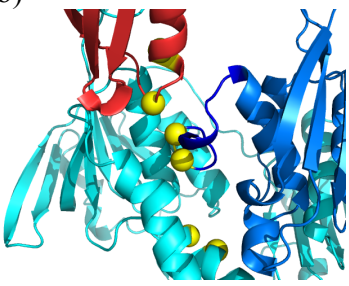

(c)

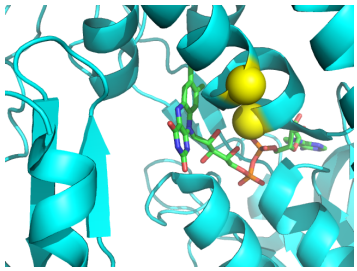

Figure I3. Structure of mercuric ion reductase. Shown is the overall modelled structure of MerA based on calculated SAXS profiles for models with experimental SAXS data (Johs et al., 2011) (a), the catalytic pathway (b), and the proximity of FAD to the catalytic cysteine residues (c). The yellow spheres represent cysteine residues involved in the transfer of Hg(II) to the catalytic core. The spheres on the red domain are the NmerA cysteine pair, on the blue domain are the CTT cysteine pair, and on the cyan domain are the inner catalytic cysteine pair.

Materials and Methods

Materials

Reagents were purchased from Sigma or Aldrich. Stratagene BL21 (DE3) pLysS cells were used for transformation of the pET3d plasmid containing the catalytic core of Tn*501* MerA and the pMAL plasmid containing the maltose binding protein (MBP) tagged catalytic core of Tn*501* MerA (Ledwidge et al., 2005; Johs et al., 2011). MerA was purified on mimetic Orange-3 resin from Prometic Biosciences. Roche protease inhibitor cocktail tablet was utilized in MerA purification.

Expression of MerA core and MerA-MBP core

Expression of the catalytic core of MerA was completed by picking a colony from transformed BL21 (DE3) pLysS cells plated on Amp/Cm plates containing 1 μL/mL of 100 mg/mL of ampicillin and 34 mg/mL chloramphenicol. The colony was used to inoculate 200 mL lysogeny broth (LB) cultures containing 1 mL of ampicillin (100 mg/mL) and chloramphenicol (34 mg/mL) (Amp/Cm) for overnight growth at 37 °C. A liter of culture was inoculated with 25 mL of the overnight culture.

The cells containing the MerA catalytic core gene were grown to an optical density at 600 nm (OD_{600}) of 0.7 at 37 °C and induced with 400 μM isopropyl β-D-1-thiogalactopyranoside (IPTG) and grown for an additional 4 hours. The cells containing the MerA-MBP plasmid were grown to OD_{600} of 0.5

at 37 °C and the temperature was dropped to 17 °C and induced with 400 μM IPTG at OD_{600} of 0.7 and grown for an additional 16 hours.

Purification of MerA core and MerA-MBP core

Cells were pelleted (6500 rpm for 15 min in SLC 6000 rotor) and resuspended in 20 mL Prep buffer (50 mM potassium phosphate (KP_i), pH 7.3, 10 mM β-mercaptoethanol (BME), 1 mM ethylenediaminetetraacetic acid (EDTA)). Added to the resuspended cells were 100 μM flavin adenine dinucleotide (FAD), 1 mg deoxyribonuclease (DNase) I, and 1 protease inhibitor cocktail tablet. Cells were then sonicated with 6.5 pulsation power on for 1 second and off for 1 second for a total of 1 minute. Cell debris was pelleted by ultracentrifugation at 47000 rpm for 1 hour. Supernatant was diluted to 400 mL with Prep buffer.

MerA catalytic core was applied to an Orange-3 affinity column (5.5 x 4 cm) and washed with 1 L of Prep buffer. The protein was eluted with 200 mL of Prep buffer containing 1 mM nicotinamide adenine dinucleotide phosphate ($NADP^+$). This was followed by a Sephacryl 200 column (2.5 x 38 cm) equilibrated in Prep buffer to separate proteins of differing sizes.

MerA-MBP catalytic core was purified on an amylose column and washed with 1 L of Prep buffer. MerA-MBP was eluted with 10 mM maltose. The MBP was cleaved off by overnight digestion with 3C protease at 4 °C. MerA was purified away from MBP by the Orange-3 column described for MerA above.

To remove the remainder of the $NADP^+$, MerA was concentrated and run through a Sephadex G-50 column (2.5 x 43 cm) equilibrated with Prep buffer

containing 2 M urea at room temperature. The protein was then concentrated to 3 mL with 50 μM FAD, and the protein was applied to a Sephadex G-50 column (1.5 x 25 cm) equilibrated with 50 mM KP_i, pH 7.3. Aliquots of MerA were then stored at -80 °C in 10% glycerol (v/v).

Steady-State Kinetics

Steady-state experiments were completed on an Uvikon XL spectrophotometer with a temperature-controlled cell holder. Experiments were carried out at 25 °C. The rates of the reactions were determined by the disappearance of the NADPH absorbance at 340 nm ($\Delta\varepsilon_{340}$ = 6.2 mM^{-1} cm^{-1}). Curves were analyzed using KaleidaGraph. The reaction mixtures consisted of 50 mM KP_i at pH 7.3, 50 μM NADPH, and 50 nM Tn*501* MerA core. The concentration of $Hg(SG)_2$ was varied from 2.5 μM to 250 μM. All reagents were premixed in a cuvette, and the reaction was initiated with the addition of the $Hg(SG)_2$ complex. A Michaelis-Menten curve was fit to the data to determine the maximal velocity k_{cat} and the Michaelis constant $K_{M\text{-}Hg}$:

(M1)

$$\vartheta = k_{cat}[S]/(K_{M-Hg} + [S]).$$

To determine the dependence of $k_{cat}/K_{M\text{-}Hg}$ on the concentration of GSH, a series of steady-state experiments with varying concentrations of GSH from 1 mM to 15 mM were collected.

Pre-equilibrium Kinetics

Pre-equilibrium rates for the binding of Hg(II) on the Tn*501* MerA core C-terminal tail were completed using a Hi-Tech Scientific SF-61 DX2 Double Mixing Stopped-Flow spectrofluorometer. The experiment was initiated by mixing 75 μL of 10 μM MerA in 50 mM KP_i with 75 μL of $Hg(SG)_2$ in concentrations ranging from 50 μM to 1000 μM prior to 2-fold dilution from mixing in the temperature regulated observation cell, which was maintained at 25 °C. Hg(II) binding was monitored by an increase in the FAD fluorescence that has been shown to be associated with neutralization of the C464 thiolate (Tn*501* catalytic core numbering used throughout), either by protonation or binding of Hg(II) (Ledwidge et al., JACS 2005). A wavelength of 450 nm was used for excitation of the FAD fluorescence, which was then monitored with an emission filter with a 495 nm cutoff.

The resulting exponential fluorescence curves were fit to either of two equations:

(M2)

$$F = Ae^{-kt} + C$$

or

(M3)

$$F = A_1e^{-k_1t} + A_2e^{-k_2t} + C$$

where A is the amplitude, *k* is the observed rate constant, and C is the background fluorescence. Best fits were obtained by iteratively implementing the Levenberg-Marquardt algorithm in KaleidaGraph using differing initial guesses.

The rates obtained from the exponential fits were then plotted against the concentration of $Hg(SG)_2$. A linear or hyperbolic curve was fit to these data to obtain the apparent second order rate constant for initial reaction of MerA with $Hg(SG)_2$ or the k_{max} and $K_{1/2}$, respectively. A linear fit of the data

(M4)

$$k_{obs} = k_1[Hg(SG)_2]$$

would be expected in the case where a fluorescence change occurs in the first step of the reaction (Figure M1a), while a hyperbolic fit of the data

(M5)

$$k_{obs} = \frac{k_3[Hg(SG)_2]}{K_{1/2} + [Hg(SG)_2]}$$

would be expected in the case where the fluorescence change occurs in the second step of the reaction (Figure M1b).

Fluorescence pKa Experiments

The Hi-Tech Scientific SF-61 DX2 Double Mixing Stopped-Flow spectrofluorometer was also used to determine the fluorescence of the Tn*501* MerA core at differing pH to elucidate the apparent pK_a values of the residues involved in fluorescence quenching. Similar to the pre-equilibrium experiments, excitation of the FAD fluorescence was accomplished with a 450 nm wavelength, and the fluorescence was monitored using a 495 nm cutoff emission filter. The protein solution contained 10 μM MerA in 10 mM KP_i at pH 6.0.

In the stopped-flow observation cell, 75 μL of buffered MerA were mixed with 75 μL of buffer (0.2 M MES, 0.1 ethanolamine, and 0.1 M triethanolamine)

at varying pH from 4 to 11 at 25 °C. Data was collected until the fluorescence stabilized, which was recorded as the final fluorescence for the given pH. The 100% fluorescence response was set by the pH 4 reading.

Nuclear Magnetic Resonance Spectroscopy

The ^{13}C-^{1}H HSQC (Kay et al., 1992) NMR experiments were completed on a Bruker Avance 800 MHz spectrometer with cryogenic four-channel probes. The ^{15}N-^{1}H HSQC NMR experiments were completed on a Bruker Avance 500 MHz spectrometer.

Isotopic labeling of MerA was completed growing cells in M9 minimal media and adding 50 mg L^{-1} of ^{13}C-methyl α-ketobutyric acid and 100 mg L^{-1} of ^{13}C-dimethyl α-ketoisovaleric acid (Cambridge Isotopes) at an OD_{600} of 0.5.

For both experiments the protein concentration was 150 μM in D_2O containing 50 mM KP_i. The NMR data were analyzed using NMRPipe (Delagio *et al*. 1995). NMR spectra figures were developed using Sparky (T.D. Goddard and D.G. Kneller, University of California, San Francisco) (Aglietti et al., 2013).

Sequence Alignment

CLUSTAL X was used to align the 5 diverse sequences found from a BLAST search of the *Bacillus* MerA sequence (Larkin et al., 2007; Altschul et al., 1990). A gap opening penalty and gap extension penalty of 10.0 and 0.2, respectively, were used. There was no manual correction performed on the alignment as to decrease the subjectivity of the assessment.

FloppyTail Simulations

The Rosetta protocol FloppyTail was implemented to simulate the dynamic behavior of the C-terminal tail (CTT) of MerA. The protocol uses a combination of Monte Carlo and minimization steps to sample the conformational space of the CTT. The Tn*501* structure of MerA was used in the simulations, with the position of the CTT randomly seeded for each simulation.

Preliminarily, a 1000-step centroid simulation was implemented as a computationally efficient means of pushing the tail toward the lowest energy well using small, shear, and minimization moves. This was followed by a 1000-step all-atom simulation that is initiated with the lowest energy structure from the centroid simulation and uses small, shear, repack, minimization, and rotamer moves. The final output of the simulation consists of poses of the structure throughout the simulation and the lowest energy structure from the all-atom simulation. A chart depicting the steps involved in the simulation is shown in Figure M2.

We used the distance between the Y441 and terminal G467 Cα atoms as a metric for the flexibility of the CTT. Tyrosine 441 is a dimer cleft-centric residue that provides a reasonably unbiased distance between that CTT and the dimer cleft (Figure M3). The wild-type enzyme, in addition to the *in silico* mutants K99M, E446Q and K449M, were analyzed for tail flexibility.

(a)

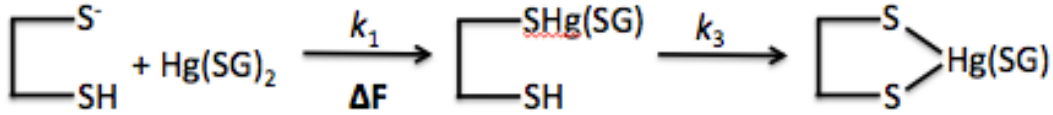

(b)

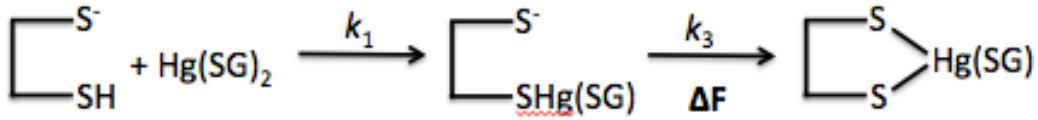

Figure M1. Models of fluorescent changes during the acquisition of Hg(II) by the CTT of MerA. Here we would expect a linear concentration dependence (a) and a hyperbolic concentration dependence. The **ΔF** indicates the location of the fluorescence change.

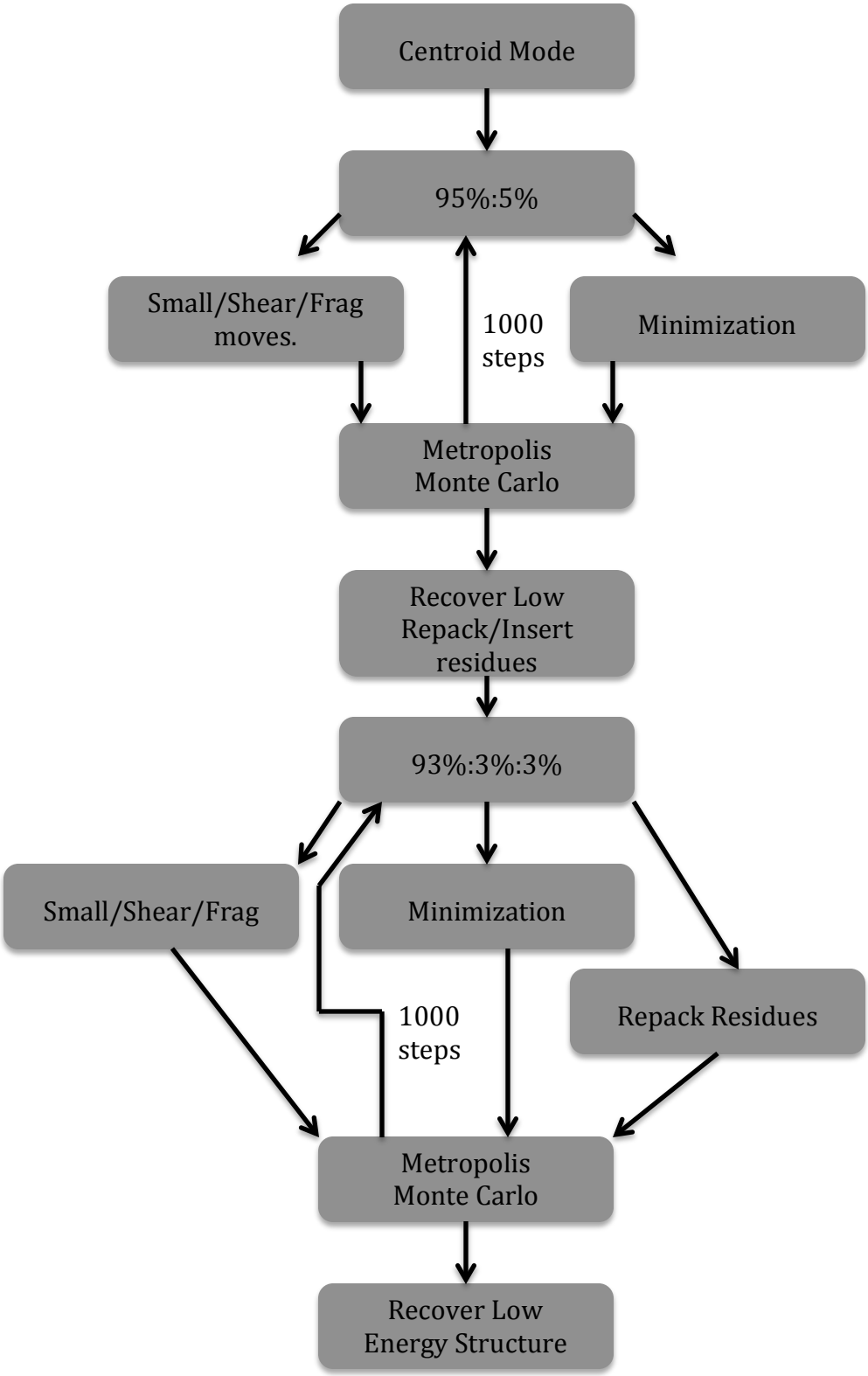

Figure M2. FloppyTail protocol tree.

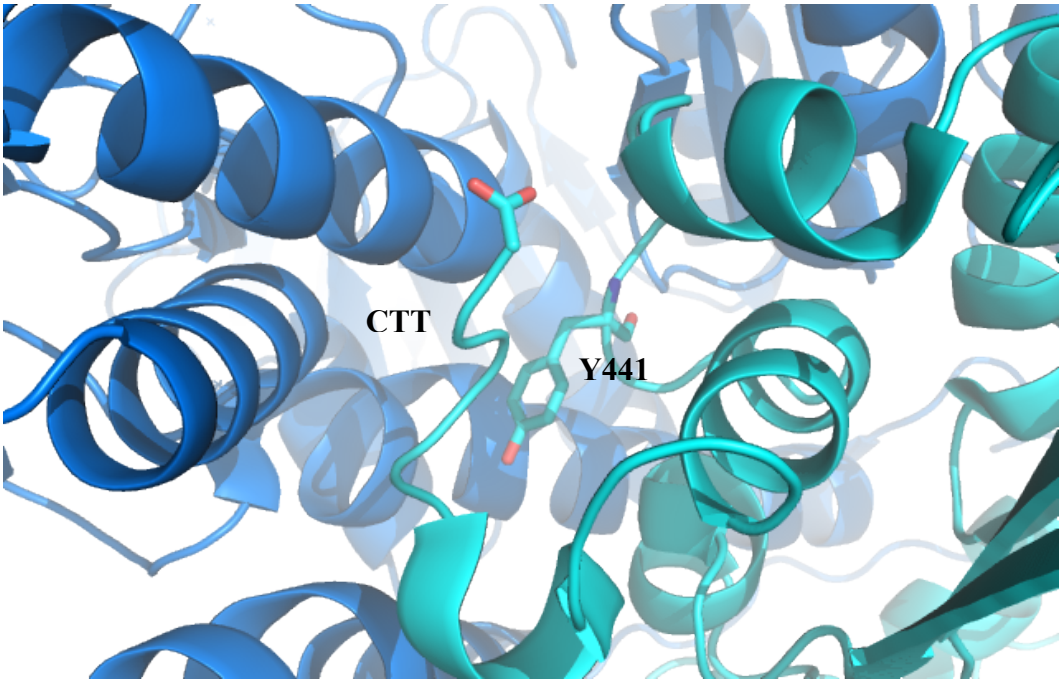

Figure M3. Image of the centric location of residue Y441. The C_α atom of this residue and of the C-terminus were used as pivot points for the distance metric of the CTT in the Rosetta FloppyTail protocol.

Chapter 1:
Rosetta FloppyTail Simulations of the MerA Carboxy-terminal Tail

Abstract

As discussed below, there exist many conserved amino acids surrounding the MerA CTT in the dimer cleft. We used *in silico* mutations along with the Rosetta protocol FloppyTail (Kleiger et al., 2009; Crawley et al., 2010) to identify the amino acids that may play a significant role in the modulation of the MerA CTT dynamics. Of the conserved amino acids in the dimer cleft, consisting of in part K52, Y100, Y107, K88, Y441, K99, E446, and K449 there appeared to be a minority of conserved residue types. A combination of the lowest energy structure from the FloppyTail simulations and the known conserved residues, it appeared that K99, E446, and K449 were involved in significant electrostatic interactions with the CTT.

Results and Discussion

Before running the FloppyTail simulation to gain insight into the residues possibly involved in the modulation of the MerA CTT, it was important determine which residues within in the protein possessed a high degree of sequence conservation. Figure 1.1 shows the sequence alignment of 5 diverse sequences found in a BLAST search against the *Bacillus* full-length MerA protein. The most highly (i.e., near 100 %) conserved residues have been mapped onto the MerA structure and displayed in Figure 1.2 on the *Bacillus* structure, which shows

the structure of the tail unadulterated by bound Hg(II). Since we were looking for the most conserved residues, it wasn't relevant whether we used the *Bacillus* or Tn*501* MerA sequences. In principle, important residues for modulating the tail dynamics would be conserved across all forms of MerA.

The most striking similarity of the conserved residues is their electrostatic characteristics. Although all of the residues are not of the same charge or polarity, this may at least suggest that the important residues within the protein are those critical for either catalytic activity or strong polar interactions.

With the conserved amino acids elucidated, we used the FloppyTail protocol to construct an ensemble of low energy structures of the MerA CTT in hopes of capturing the dimer cleft residues that appeared to form the most significant interactions with the CTT. Figure 1.3 shows the conformation of each of the 10 lowest energy structures from the 10, 1000-step all-atom simulations of the tail. Each low-energy state adopts strikingly similar geometries, which suggests there are well-defined energetic determinants. While the starting poses of the protein were randomly seeded, most of the structures started in the dimer cleft of the protein (Figure 1.4).

From visual inspection of the data and intuition, we found a set of three residues, referred to as the ionic triad, that are conserved, within a reasonable proximity of the tail (i.e., ca. 4 Å), and have the potential to form a traditional electrostatic interaction (i.e., oppositely-charged electrostatic pairs). These residues consist of K99, E446, and K449 from the Tn*501* structure (PDB ID 1ZK7), which is shown in Figure 1.5 (Ledwidge et al., 2005). It is important to

note that although there appears to be hydrogen bond potential between these residues and the backbone amides, hydrogen bonds depend intricately on the geometry of the interactions, which lends some skepticism to the actual interaction type.

Although the lowest energy structures provide some indication as to the residues involved in modulating the dynamics of the MerA CTT, it is also informative to look at the *in silico* change in tail populations by using informed point mutants. By using PyMol to produce point mutations in the structure coordinate files of the Tn*501* MerA, we were able to construct histograms depicting the flexibility of the CTT by using a distance metric. The metric provided the distance between the C_α atom of the C-terminal residue and the C_α atom of the Y441, where Y441 sits at a nearly central location at the bottom of the dimer cleft, thus acting as a good reference point.

We made the following point mutations: K99M, E446L, and K449M. Although alanine mutations are more common, these intelligent mutations provided similar steric properties to the wild-type residues, thus minimizing the observed differences in the mutants due to packing. The histograms of the states populated by the CTT for the wild-type protein and the mutant are shown in Figures 1.6a-c. As was expected, the histograms suggest that the tail attains greater flexibility in the absence of any of the ionic triad residues.

The tail in the K99M mutant tended to populate the wild-type distance as much or more frequently compared to the other mutations; however, the tail in this mutant also tended to populate the largest distances from the dimer cleft.

This may suggest that K99 plays a central role in allowing the tail to populate the side-docked conformation, where it has been suggested that NmerA docks during mercury transfer, shown in Figure I3a (Johs et al., 2011). Without preferentially populating the side-docked conformation, the tail may make excursions that move the tail much further from the dimer cleft.

The E446L and K449M mutations produced populations similar to wild-type; however, the tail also populated states up to 35 Å from the dimer cleft. This too suggests that E446 and K449 play intricate roles in stabilizing the tail in the dimer cleft, where efficient transfer of Hg(II) between NmerA and the inner cysteine residues can occur. If the tail was not stabilized close to the dimer cleft, the tail would more frequently make stochastic fluctuations away from the Hg(II) transfer pathway, effectively decreasing the rate of overall Hg(II) transfer from NmerA to the inner cysteine pair.

A significant caveat of this protocol is that it was not established to produce thermodynamic ensembles as a result of the built-in minimization steps and other biases. The protocol is intended to drive a given floppy tail to the global minimum energy state. As a result, the histograms of Figure 1.6 do not accurately represent a thermodynamic ensemble of states, thus an equilibrium constant could not be calculated from these data. However, the histograms do provide a sense of the allowable conformational space of the tail, as the energy difference between the *in* tail conformation and *out* tail conformation in the mutants, compared to wild-type, must be small enough to allow the Monte Carlo algorithm to sample these states given the Metropolis criterion. In general, the

Metropolis criterion makes it exponentially less likely to accept a state of higher energy in a Markov Chain as the energy difference increases.

The images of the lowest energy states for the wild-type protein in conjunction with the histograms representing the spatial states of the CTT provide a greater sense of the role of the ionic triad residues. Although there exist many caveats when implementing computational work to augment or drive wet-science, the data presented here support that K99, E446 and K449 play some role in modulating the MerA CTT dynamics.

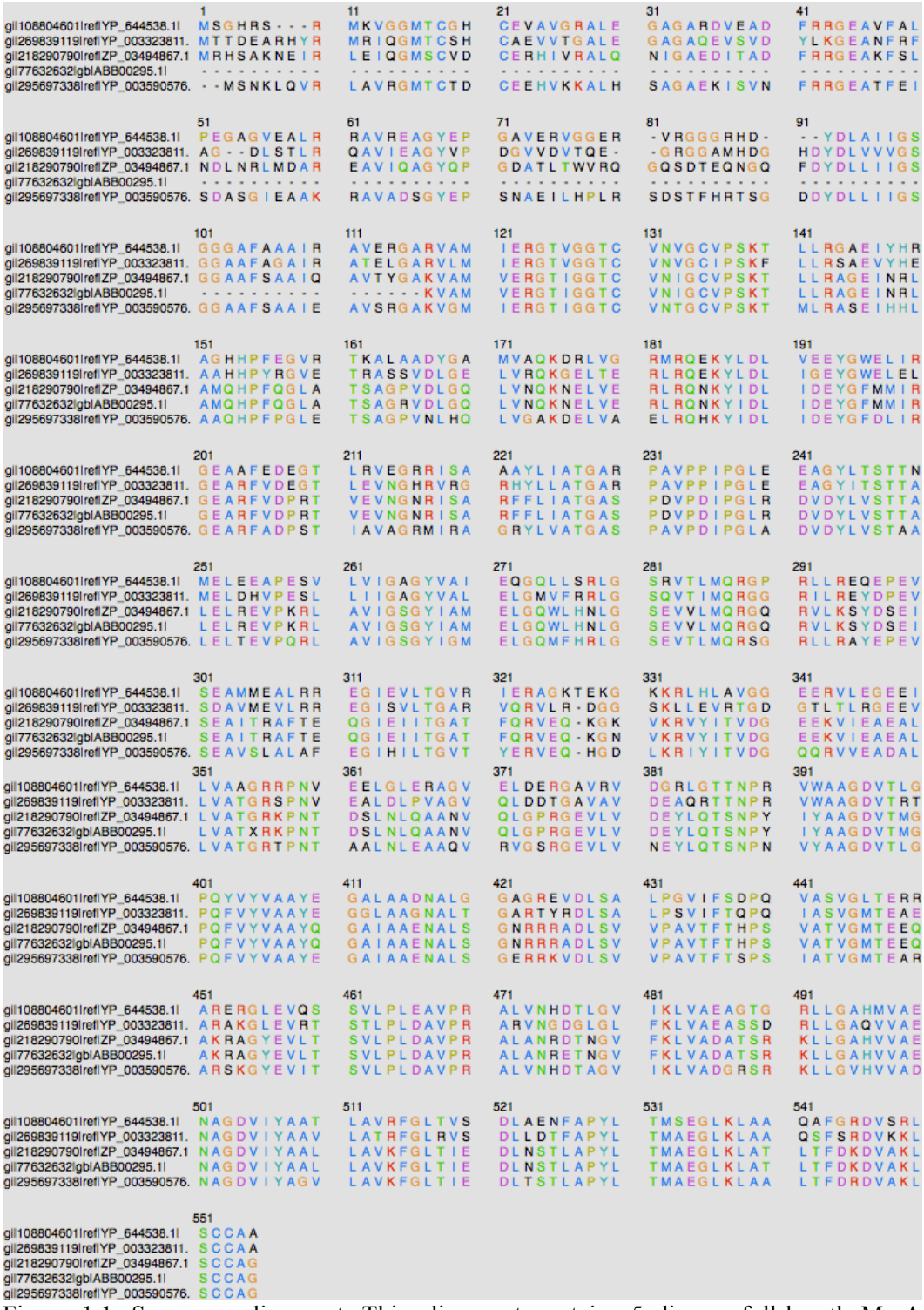

Figure 1.1. Sequence alignment. This alignment contains 5 diverse full-length MerA sequences. In order from top to bottom, the sequences consist of: *Rubrobacter xylanophilus*, *Thermobaculum terrenum*, *Alicyclobacillus acidocaldarius*, *Alicyclobacillus vulcanalis*, *Kyrpidia tusciae*. The different colors reflect minimum percentage presence for differing residue types, as defined for the Clustal X default coloring scheme. Sequences were obtained from NCBI and alignment was completed with Clustal X.

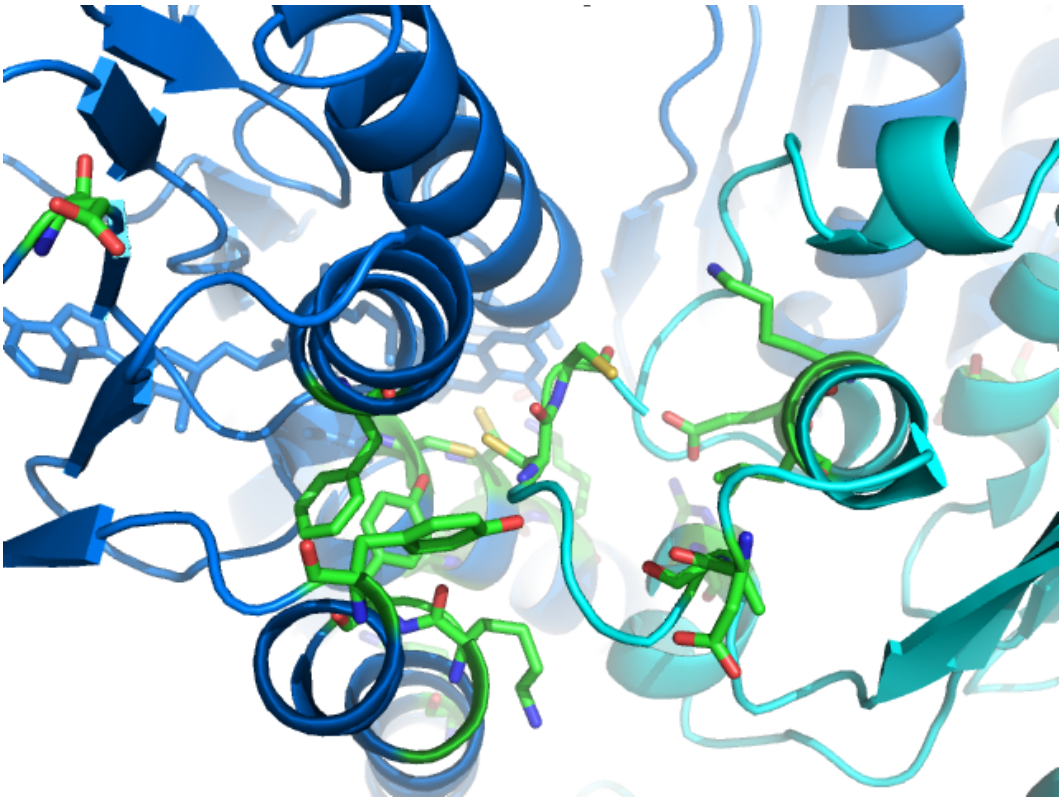

Figure 1.2. Image of conserved amino acids. These residues are within or near the dimer cleft of the *Bacillus* MerA structure. The cyan and blue chains represent the two monomers of the dimer, with the green residues representing conserved amino acids. Most of the predominantly conserved amino acids are polar or charged.

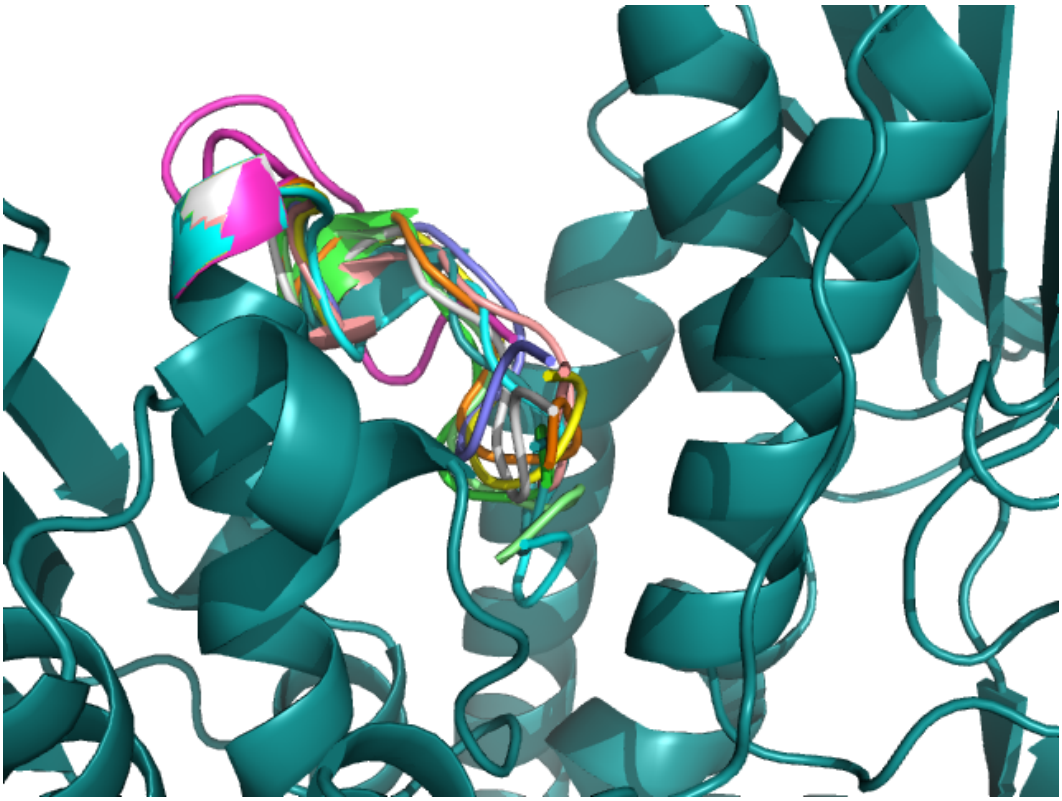

Figure 1.3. The 10 lowest energy structures from each of the FloppyTail all-atom simulations. Each pose represents a cartoon illustration of the lowest energy structure from a 1000-step all-atom simulation that was preceded by a 1000-step centroid simulation. The tail in each case adopts a similar conformation, suggesting the dimer cleft acts as a significant energy sink.

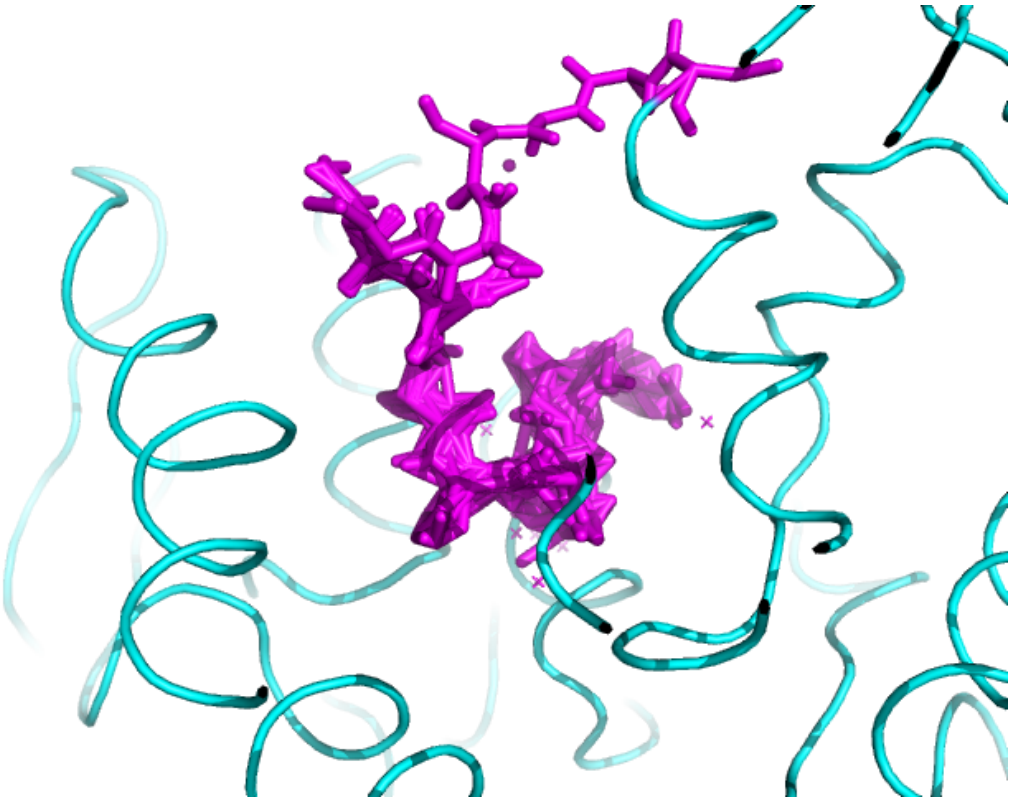

Figure 1.4. Starting structures of the CTT for the FloppyTail protocol. Although the flag *constant_seed* was false for the simulation, most of the starting poses of the structure were all still within the dimer cleft.

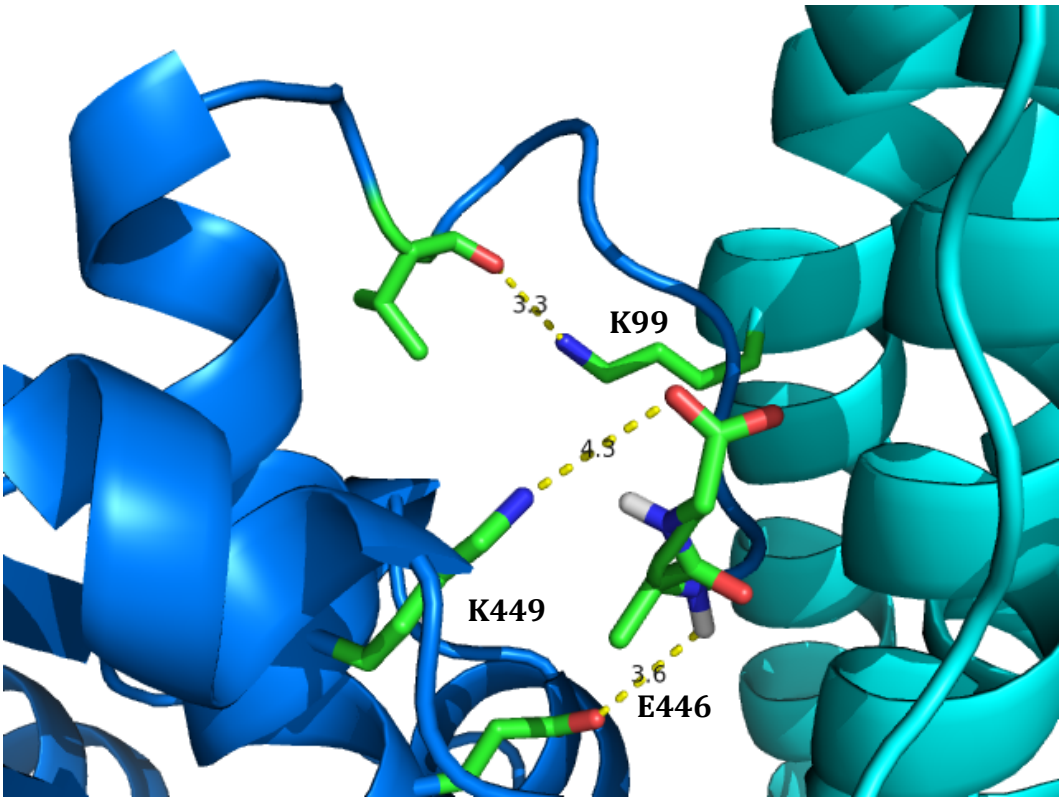

Figure 1.5. Lowest energy structure from Rosetta FloppyTail protocol. The ionic triad residues are depicted in what is postulated to be their native contacts in the absence of crystal contacts, although the overall tail structure is similar to the starting crystal structure. While each contact may not possess the correct geometry for hydrogen bonding, likely some form of electrostatic interaction exists.

(a)

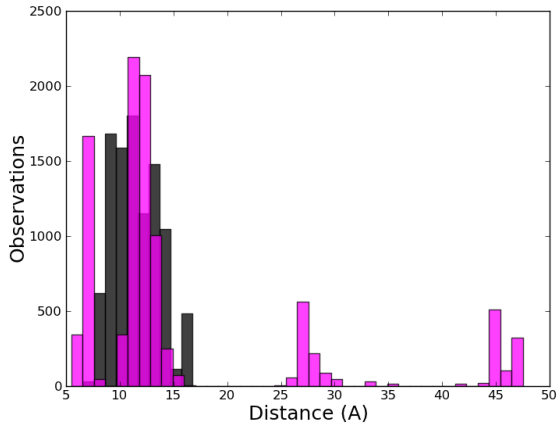

(b)

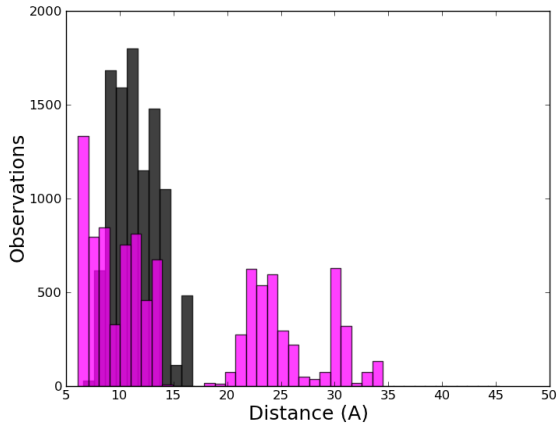

(c)

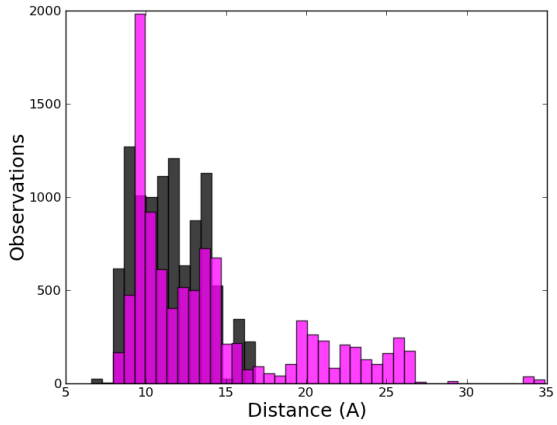

Figure 1.6. Histograms of the distance distribution of the CTT for wild-type (black) and the given point mutant (magenta). The point mutants consist of K99M (a), E446L (b) and K449M (c). The average distance populated by the tail is 11.5 Å for wild-type, 15.9 Å for K99M, 16.0 Å for E446L and 14.2 Å for K449M.

Chapter 2:
Kinetics of Hg(II) Acquisition by the MerA CTT

Abstract

Evidence suggesting flexibility of the carboxy-terminal tail (CTT) of mercuric ion reductase was first discovered in the early 1990s. Schiering et al. noticed the lack of ease in fitting the structural model to the electron density maps in the C-terminus of MerA due to the lack of well-defined electron density (1991). Based on the SAXS model of MerA, there is believed to be a nearly 20 Å to 25 Å distance that Hg(II) would need to travel from NmerA to the inner cysteine residues of the core, it can be inferred that the flexibility of the tail may play a pivotal role in the Hg(II) delivery pathway between NmerA and the inner cysteine residues where reduction to Hg(0) occurs.

While some work has been done in investigating the kinetics of mercury acquisition by MerA (Ledwidge et al., 2005), no published work exists that investigates the kinetics of Hg(II) acquisition solely by the MerA CTT.

We analyzed the transfer of Hg(II) from a $Hg(SG)_2$ complex to the MerA catalytic core using steady-state, stopped-flow, and kinetic modeling. Previous work completed with the K449A mutant and new data on the E446Q and K99A mutants are presented. As described in detail below, comparison to wild-type data suggests K99A and K449A mutations liberate the tail, while the E446Q mutation appears to constrain the tail to the dimer cleft.

Steady-State Kinetics of Ionic Triad Residues

Steady-state data collected in the presence of 1 mM GSH for the wild-type enzyme and the ionic triad mutants are shown in Table 2.1. In each case, mutation of an ionic triad residue substantially decreased the k_{cat}, suggesting that these residues either play a role in the efficient reduction of Hg(II) – where E446 may play a proton acceptor/donor role and both lysine residues may play a role in modulating pK_a values for nearby catalytic residues – or they are involved in the delivery of Hg(II) to the inner cysteines, in a direct or indirect manner. Based on the FloppyTail results and intuition, we predict that the decrease in k_{cat} results from a change in the CTT dynamics, presumably by liberating the tail so as to decrease the probability of exchange of Hg(II) between the tail and the inner cysteine residues.

Using k_{cat}/K_M as an estimation of the minimal initial second-order rate constant for $Hg(SG)_2$ acquisition by the CTT of the enzyme, both K99A and E446Q MerA appear to acquire Hg(II) more slowly, while K449A has an order of magnitude increase in the rate of Hg(II) acquisition compared to wild-type. These data suggest that at least the K449A mutation allows for liberation of the tail so that it populates an *out* state more frequently than the *in* state, where the *in* state has the tail bound in the dimer cleft and the *out* state has the tail exposed to bulk solvent. We can infer this, as with the CTT in the *out* state, the C-terminal cysteine pair would be more accessible, thus allowing for an increased rate of mercury acquisition. Since k_{cat}/K_M is only a minimal estimation of the second-

order rate constant, we cannot propose a confident statement with regards to the effects of the K99A and E446Q mutations.

These data are promising as they are not yet inconsistent with our FloppyTail results obtained from our computational work. To further expand our knowledge of the kinetics of Hg(II) acquisition by the CTT, we parsed the individual rates of acquisition out of the existing kinetics data using mathematical models developed from the predicted model of Hg(II) acquisition by the CTT of MerA.

Dependence of k_{cat}/K_M on GSH Concentration

Most steady-state parameters are rather difficult to interpret and somewhat ambiguous. As a result, mathematical models of the physical model of Hg(II) acquisition by the CTT were derived for the model shown in Figure 2.1. These mathematical models provide a set of the individual rates, or ratio of rates, for the simple two-step mercury acquisition model. The model contains a competitive inhibitor step, where $Hg(SG)_2$ equilibrates with $Hg(SG)_3^-$ (K_d=24.1 mM is the pH-corrected value for pH 7.3, Cheesman et al., 1988), before proceeding down the Hg(II) acquisition pathway involving an initial attack and displacement of a GSH molecule by the more accessible C-terminal cysteine, followed by attack of the thiolate cysteine and displacement of the second GSH molecule.

In the case where neither the first step nor the second step of the model in Figure 2.1 is reversible, the following equation would be relevant:

(2.1)

$$k_{cat}/K_M = \frac{k_1}{\left(1 + \frac{[GSH]}{24.1}\right)},$$

where [GSH] is given in mM here and below. If only the first step of the model were reversible, we have:

(2.2)

$$k_{cat}K_M = \frac{k_1}{((\frac{k_2}{k_3}[GSH] + 1)(1 + \left(\frac{[GSH]}{24.1}\right))}.$$

Finally, with both the first and second steps of the reaction reversible, we have the following equation:

(2.3)

$$k_{cat}K_M = \frac{k_1(1 + \left(\frac{[GSH]}{24.1}\right))}{(\left(\frac{k_2}{k_3}[GSH] + 1\right) + (\left(\frac{k_2 k_4}{k_3 k_5}\right)[GSH]^2)}.$$

The best fitting of these models for wild-type, K99A, E446Q, and K449A are shown in Figure 2.2. Both wild-type data and E446Q fit to equation 2, suggesting only the first step of the Hg(II) acquisition is reversible, while K99A and K449A fit to equation 3, suggesting both steps of the Hg(II) acquisition model are reversible.

Preliminary analysis of the fits further support the steady-state parameters by indicating that the E446Q mutant acts similar to wild-type protein but constrains the tail dynamics even further. That is, with the tail of the protein packed securely in the dimer cleft, we would predict the access of glutathione to

the Hg(II) bound by the CTT cysteine pair would be hindered even more, preventing reversibility, which we do observe. These data also support the steady-state parameters for K449A, which suggested that the K449A mutantation liberates the CTT, thus increasing rates of Hg(II) acquisition and would induce reversibility of both steps in the model due to increased the accessibility of GSH to the C-terminal cysteine residues. In contrast, these data confuse the steady-state parameters by supporting the initial hypothesis that the K99A mutant helped to liberate the tail, which is suggested by the better fit to equation 3 where both steps of the simple model are reversible, indicating increased accessibility by GSH. However, the steady-state parameters for the K99A mutant suggested that Hg(II) may be acquired more slowly by this mutant, indicating a more constrained tail.

Parameters from these fits are shown in Table 2.2. Again, these rate constants and rate constant ratios support the notion that the glutamine mutation of E446 constrains the CTT to the dimer cleft, as evidenced by the decrease in k_1 and increase in the ratio of k_2/k_3 compared to wild-type. An increase in the ratio of k_2/k_3 suggests that k_3 may have also decreased, which is supported by an accessibility argument. Similarly, the liberation hypothesis for K449A is further supported by the increase in both k_1 and k_2/k_3. An increase in k_2/k_3 for the K449A mutant may result from an increase in k_2 due to enhanced reversibility in the Hg(II) acquisition from a liberated CTT, or there could also be a differential increase in k_2 and k_3. The alanine mutant of K99 still provides some confusion as k_1 decreased compared to wild-type, which would not be expected in the case of a

more liberated CTT. However, the ratio k_2/k_3 does increases for K99A, perhaps for similar reasons as the increase in k_2/k_3 for K449A, suggesting greater reversibility of the acquisition pathway.

Another GSH concentration dependence to note is the dependence of K_M on [GSH] (Figure 2.3). Interestingly, the K_M, which is a loose measurement of the unbound substrate concentration, increases at a much faster rate for K99A MerA than either the wild-type enzyme or E446Q MerA. In fact, the sensitivity of the K_M for K99A MerA is quite similar to the sensitivity of the K_M for K449A MerA. This is indicative of GSH having a greater effect on the ability of Hg(II) to bind to the C-terminal cysteines, which would indicate that the CTT is more exposed to bulk solvent where GSH would have greater accessibility to the C-terminal cysteine residues. This corroborates our hypothesis that K99 acts in a similar function to K449, which is to shift the equilibrium of the CTT to the *in* conformation, as opposed to the *out* conformation.

Stopped-flow Fluorescence

To better elucidate the individual rate constants for the basic kinetic model shown in Figure 2.1, we utilized stopped-flow spectrofluorometry. Given the fluorescent properties of the bound FAD co-factor in MerA, where a fluorescence increase in FAD is observed on binding Hg(II) to the C-ter cysteines (Ledwidge et al., 2005), we are able to monitor the acquisition of Hg(II) by MerA in a pre-equilibrium environment.

The fluorescence traces for the MerA core mixed with $Hg(SG)_2$ in the stopped-flow instrument are shown in Figure 2.4. The traces consist of the wild-type enzyme, K99A, E446Q, and K449A. Each trace within the plots is either the background fluorescence (i.e., enzyme vs buffer), or reaction with final concentrations of 25 μM $Hg(SG)_2$, 50 μM $Hg(SG)_2$, 100 μM $Hg(SG)_2$, 150 μM $Hg(SG)_2$, 250 μM $Hg(SG)_2$, or 500 μM $Hg(SG)_2$.

Each of the mutant forms of MerA react completely with $Hg(SG)_2$, as evidenced by the 100 % fluorescence response for each fluorescence trace. The wild-type fluorescence traces are similar to those observed with $Hg(Cys)_2$ reactions, suggesting a similar reaction pathway occurs with $Hg(SG)_2$. Each mutant, however, has interesting characteristics. Most obviously, the intial quenching of fluorescence is diminished in all cases relative to WT, indicated by the increased baseline fluorescence at the beginning of the observation. The origins of these changes will be discussed later in the pK_a modulation section. Another notable effect of the mutants is the substantially increased rate of Hg(II) acquisition by K449A MerA (Figure 2.4d). It is difficult to decipher the exponential curvature of the traces due to noise in the data and the majority of the reaction occurs in the instrument dead time (ca. 1.5 ms) for this mutant. Conversely, E446Q MerA acquires Hg(II) much slower than the wild-type enzyme, as can be seen by the increase in time scale for the E446Q MerA traces to acquire 100 % fluorescence (Figure 2.4c). Finally, K99A MerA data is difficult to interpret by observing the simple stopped-flow fluorescence traces for two reasons: (1) the data is noisy and (2) the total observable fluorescence change

is only circa 4 % (Figure 2.4b). This adds difficulty to obtaining accurate fits to the data and observing the precise dead time of the reactions. At most, a 1.5 % response occurs in the dead time of the reaction, which is faster than wild-type, but it does not appear to be faster than K449A MerA, suggesting the acquisition of Hg(II) by the CTT of MerA is enhanced in the K99A mutant.

Based on the simple model of Hg(II) acquisition by MerA shown in Figure M1, we expected a single exponential (equation M2) would fit the fluorescence traces for wild-type and all point mutants, as there is only one fluorescence change step. This is true for wild-type MerA reacting with $Hg(SG)_2$ concentrations greater than at least 50 μM and not true for the E446Q or K449A data. Wild-type enzyme reacting with 25 μM and 50 μM $Hg(SG)_2$ and all concentrations of $Hg(SG)_2$ reacting with E446Q MerA produced fluorescence traces that fit best, based on the residuals of the fit, to double exponentials (equation M3).

While it is easy to imagine a different model of Hg(II) acquisition for E446Q and K449A MerA, which resulted in two separate observed rate constants for all concentrations of $Hg(SG)_2$, it is difficult to imagine why there is a concentration dependence for the number of observed rate constants observed for Hg(II) acquisition by the wild-type enzyme. This is especially true since the observed rate constant that apparently disappears at higher concentrations of $Hg(SG)_2$ is also the observed rate constant that shows a increasing trend in amplitude, suggesting the observed rate constant is becoming more significant. To rationalize this, we believe the two observed rate constant converge, such that

it is difficult to parse the observed rate constants in a fit to the raw fluorescence traces. With this being the case, we fit the observed rate constants in a $Hg(SG)_2$ concentration dependence curve as if all except the first two data points had the same observed rate constants (Figure 2.5a).

Both rates observed for E446Q and K449A MerA are also plotted in Figure 2.5. However, the additional rate observed suggests no clean concentration dependence. While we do still believe that the two rates observed in all forms of MerA are real, it is difficult to intuit what second rates observed for E446Q and K449A are derived from. Kinetic modeling would likely elucidate the origins of the second rate, which we discuss later.

From the rates believed to be associated with Hg(II) binding to the CTT, the derived rate constants are listed in Table 2.3. These rates were derived from a simple set of equations. First, a hyperbolic dependence of the observed rate constants on $[Hg(SG)_2]$, consistent with model (b) in Figure M1, results in

(2.4)

$$k_{obs} = \frac{k_3[Hg(SG)_2]}{[Hg(SG)_2] + K_{1/2}},$$

where k_3 and $K_{1/2}$ can be obtained. Second, k_3 and $K_{1/2}$ can be used to derive k_1 through

(2.5)

$$K_{1/2} = \frac{k_2[GSH] + k_3}{k_1},$$

where free [GSH] released during ligand exchange is very small, rendering the k_2[GSH] term negligible. Finally, the steady-state models resulted in the following relationship, which allows for determining k_2:

(2.6)

$$p = \frac{k_2}{k_3}.$$

As was suggested in the original hypothesis from the FloppyTail simulations, the CTT in the K99A and K449A mutants appears to be more liberated. This is indicated by the substantial increases in k_1, k_2 and k_3. If the tail is exposed in bulk solvent, the accessibility of the C-terminal cysteines is much greater, which allows for higher rates of acquisition (i.e., k_1 and k_3), which can be argued to be a consequence of less steric hindrance in both cases, and reversibility (i.e., k_2) as a result of exchange between GSH and the bound Hg(II). Conversely, E446Q MerA, as indicated by the steady-state data, acquires Hg(II) much slower than wild-type, suggesting that the CTT may be more constrained to the dimer cleft in the *in* conformation, slowing the rate of exchange of Hg(II) onto the C-terminal cysteine pair. As a result of the slow acquisition of Hg(II) by E446Q MerA, only the linear portion of the hyperbolic concentration dependence (Figure 2.5c) on the concentration of $Hg(SG)_2$ was observed for this enzyme. This only allowed for determination of k_1, which was estimated to be 30.8 mM^{-1} s^{-1}, much slower than wild-type k_1 of 256 mM^{-1} s^{-1}.

Interestingly, the rate constants derived from the stopped-flow spectroscopy differ from the steady-state results by a larger margin than mere error. We believe this may be an artifact of a difference in the overall reaction

between the two experiments. In the steady-state, both the C-terminal cysteines and the inner cysteine residues are reduced, while in the stopped-flow experiment, only the C-terminal cysteines are reduced. As a result, the steady-state experiments are complicated by the complete turnover of Hg(II) to Hg(0). The stopped-flow experiments, therefore, may provide a different representation of the isolated exchange between the cysteines of the CTT and Hg(II), which may explain the observed discrepancy.

Insights From pK_a Values

As mentioned, it has been shown that negative charges in the dimer cleft of MerA act to quench the FAD fluorescence (Engst and Miller, 1998; Engst and Miller, 1999; Ledwidge et al., JACS 2005). The large majority of the fluorescence quenching has been associated with the negative charge of C464 on the CTT. However, it was also determined that the Y100 plays a role in quenching FAD fluorescence as well (Malone and Miller, unpublished results), which results in two separate pK_a values, a lower pK_a attributed to the C464 and a higher pK_a value attributed to the Y100 (Ledwidge et al., JACS 2005).

Table 2.4 lists the pK_a values determined from fitting pK_a equations to the Fluorescence vs. pH graphs shown in Figure 2.6. The equations used assume either two or three pK_a values, respectively:

(2.7)

$$F = \frac{100 + A_1(10^{pH-pK_{a,1}}) + A_2(10^{2pH-pK_{a,1}-pK_{a,2}})}{1 + 10^{pH-pK_{a,1}} + 10^{2pH-pK_{a,1}-pK_{a,2}}}$$

and

(2.8)

$$F = \frac{100 + A_1(10^{pH-pK_{a,1}}) + A_2(10^{2pH}) + A_3(10^{3pH-pK_{a,1}-pK_{a,2}-pK_{a,3}})}{1 + 10^{pH-pK_{a,1}} + 10^{2pH-pK_{a,1}-pK_{a,2}} + 10^{3pH-pK_{a,1}-pK_{a,2}-pK_{a,3}}}.$$

The p$K_{a,3}$ values, although some slightly lower than expected, are attributed to the Y100. The value increases on mutation of the lysine residues, which suggest the positive charge lowers the pK_a by stabilization of the negatively charged hydroxyl group.

The p$K_{a,2}$ values are strikingly low, except in the mutants of the ionic triad residues. We believe that at least K449 is stabilizing the negative charge of the C464, thus decreasing the apparent pK_a. What is perplexing, however, is that removing the glutamate, a residue expected to be negatively charged, also increases the apparent pK_a, and there are three observed pK_as in the K99A mutant. To resolve this apparent paradox, we postulate that there are, in fact, three negative charges that are quenching the fluorescence of the FAD, and we are not observing all three in each form of the protein, as the pK_a attributed to C464 is actually a macroscopic pK_a associated with two interacting residues.

We believe the lower pK_a observed for K99A is actually derived from the E446 residue. In wild-type enzyme, K99 may stabilize the negative charge of E446, lowering the pK_a beyond the observed region of pH from 4 to 11. The increase in the p$K_{a,2}$ of E446Q is actually a result of removing the E446 pK_a, and thus parsing out the C464 pK_a from the E446 pK_a.

Berkeley Madonna Modeling of Pre-equilibrium Kinetics

Reconciling the pre-equilibrium data with our presumed simple model of Hg(II) acquisition, shown in Figure M1, is difficult since we are observing deviations in the kinetic traces from the expected simple single-exponential behavior. As a result, we have used Berkeley Madonna to simulate the proposed models of Hg(II) acquisition by the CTT of MerA to help us better reason the origins of the kinetic behavior.

In our pre-equilibrium kinetic traces, we found that we observed two exponential phases deriving from fluorescence changes during Hg(II) acquisition by the CTT of MerA. As shown in Figure 2.5a, one of the observed rate constants shows simple hyperbolic concentration dependence with a zero y-intercept. This is presumed to result from the first-order quenching of the fluorescence upon Hg(II) binding the C-terminal cysteine with the lower pK_a in the second step of the scheme in Figure M1b. Interestingly, the second observed rate constant has a linear concentration dependence, suggesting that the observed fluorescence change occurs in or is preceded by a rate-limiting second-order reaction (Figure M1a). These rates also have a non-zero y-intercept, which suggests that the step is reversible or there exists an intermediate transient fluorescent species that is fluorescent and proceeds on in the reaction to a non-fluorescent species.

With these characteristics in mind, we developed a set of three kinetic models with varying degrees of complexity and goodness of fit. Each model contained the same set of principles where there existed at least the simple model of Hg(II) acquisition shown in Figure M1b in addition to a separate pathway

where a fluorescence change could be brought about by an alternative binding or acquisition mode.

The Pre-Binding model of Figure 2.7a involves a primary acquisition pathway involving the metal binding of Hg(II) to the more accessible cysteine followed by formation of a reversible 3-coordinate complex with the negatively charged cysteine, and ultimately loss of the second GSH ligand and the final chelation of Hg(II) by the two C-terminal cysteines. This process should give rise to the hyperbolic concentration-dependence. The apparently reversible reaction giving the linear concentration dependence arises in this model from the formation of a pre-binding complex between $Hg(SG)_2$ and MerA that involves thermal fluctuations of the $Hg(SG)_2$ complex prior to the appropriate geometry for attack from the CTT is attained. This pre-binding complex could involve an excursion of the CTT out of the cleft, resulting in an initial fluorescence change, and a subsequent attack of the lower pK_a cysteine on the mercury of the $Hg(SG)_2$ complex.

The best global fit to the data using this model is shown in Figure 2.8a. The higher concentrations of $Hg(SG)_2$ fit better than the lower concentration traces where the model is predominantly single-exponential while the data exhibit double exponential behavior. Analysis of the rate constants suggests that the top pathway is the primary acquisition pathway, while the fluorescent pre-bound complex traps a fraction of the Hg(II), where it can slowly be recovered by the CTT and proceed to the fully chelated complex.

The second model, shown in Figure 2.7b, is the CTT equilibrium model. This model mirrors the pre-binding model, except the alternative binding pathway does not derive from an equilibrium between a bound $Hg(SG)_2$ complex and the unbound complex but rather between the *in* and *out* state of the CTT, where a fluorescence change is only observed in the steps involving Hg(II) binding to the negatively charged thiol.

The global fit of this model to the raw kinetic traces, shown in Figure 2.8b, is a nearly perfect fit to the data. However, kinetic constants giving the best fit result in an equilibrium between the *in* and *out* conformations of the tail that is not physically real. By allowing the starting concentrations of the *in* and *out* conformations to vary, the *in* conformation is 3.7 μM and the *out* conformation is 1.3 μM. However, the rate constants for the *in* to the *out* conformation is 41 s^{-1} and the reverse is 1 s^{-1}. Since the following relationship exists between rates and concentrations in an equilibrium:

(2.9)

$$K_{eq} = \frac{[A]}{[B]} = \frac{k_2}{k_1},$$

where A and B are two states and k_1 and k_2 are the forward and reverse rates, respectively, between the two states, the fact that the forward rate constant is so much higher than the reverse rate constant is not congruent with the higher initial concentration of the *in* conformation. As a result, although the model is intuitive and we can obtain good fits to the kinetic data, the actual rates are not physically realistic. Forcing the rate constants to be consistent with the concentrations, or

concentrations to be consistent with the rate constants, leads to loss of the double exponential character of the fits.

To resolve this issue, we examined a more complicated model involving a 4-coordinate complex (Figure 2.7c). This model, mirrors the CTT equilibrium model with the addition of initial 3-coordinate complexes for both of the acquisition pathways that can equilibrate with each other through a 4-coordinate complex.

The global fit of this model (Figure 2.8c) is not as good as the simple CTT equilibrium model; however, the characteristics of the fit are similar to the kinetic traces, and the relationship between the concentration of the *in* and *out* conformations and the rate constants between the states is resolved. Here, the concentration of the *in* conformation is 2.6 μM and the *out* conformation is 2.7 μM, and the rate constant from *in* to *out* is 30 s^{-1} and the reverse is 31 s^{-1}; therefore, the relationship in equation 2.9 holds true for this model. The remaining rate constants in the model are also consistent with a real physical model, yet an interesting aspect of this model is the concentrating of the reaction into the 4-coordinate complex. It is possible that the off-pathway 4-coordinate complex is semi-stable and does form along the reaction pathway. Another interesting issue is the final rate constant leading to the 2-coordinate, fully chelated complex is lower than k_{cat}, which as discussed earlier, could be explained by the fact that the mechanism of Hg(II) acquisition is altered in the stopped-flow experiments where the inner cysteine residues are oxidized rather than reduced as in turnover.

While these four models are not comprehensive, they represent a set of the models consistent with the observed kinetic behavior between wild-type MerA and $Hg(SG)_2$. The fit of the models to the raw data is reasonable, but likely the real model of $Hg(SG)_2$ acquisition by the CTT of MerA remains elusive. That is not to suggest that our models of Hg(II) acquisition are grossly inaccurate. The idea of two separate Hg(II) acquisition pathways is consistent with our observations of the fluorescent changes. Small changes in the existing models along with better initial estimations of the rate constants would likely result in better fits between the models and the raw fluorescent traces. It is interesting to note that in previous studies of Hg(II) acquisition by the CTT result in simple single-exponential behavior at all HgX_2 concentrations, yet the glutathione complexes of Hg(II) change the characteristics. Additional modeling and experimentation will need to be completed to resolve this issue.

Conclusions on the Kinetics of Hg(II) Acquisition

While we will develop our complete understanding of the CTT mechanism in chapter 4, the kinetic data, both steady-state and pre-equilibrium, support the notion that E446Q MerA decreases the accessibility of the CTT to the surface of the protein and K449A MerA increases the accessibility of the CTT to the surface of the protein where Hg(II) acquisition can occur more freely.

The kinetic data for K99A MerA is not fully resolved. The reversibility of both acquisition steps from the simple model, as indicated by the GSH concentration dependence of k_{cat}/K_M, and the high rates for k_1, k_2 and k_3

determined from the combined stopped-flow data and GSH dependence suggest that the K99A mutation increases the accessibility of the CTT to the surface of the protein for enhanced rates of Hg(II) acquisition. The k_{cat}/K_M determined from the reaction of K99A MerA and $Hg(SG)_2$ at 1 mM GSH, which can be used as an estimation for the second-order rate constant, is similar to E446Q, suggesting a lower rate of Hg(II) acquisition, thus a more constrained CTT; however, this is only a minimal estimation of the second-order rate constant, thus does not strongly argue a more constrained CTT. Perhaps the most convincing data strongly suggesting that there is increased liberty of the CTT in the K99A mutant of MerA is the pattern of K_M values observed over the change in [GSH] (Figure 2.3). The high sensitivity of the K_M to the GSH concentration is highly similar to that observed for K449A MerA. This is strongly supportive of the liberation of the CTT in K99A MerA.

Given the rationalization of the effects of K99 on the rate of Hg(II) acquisition by the CTT, we can state that the lysine residues of the ionic triad are stabilizing the tail in the dimer cleft, and E446 may act in an opposing manner to help balance the energy difference such that the equilibrium between the *in* and *out* state fosters an appropriate balance between the rate of Hg(II) acquisition and hand off to the inner cysteine residues to maximize the overall turnover rate of the enzyme.

Table 2.1. Steady-state parameters for wild-type and ionic triad mutants at 1 mM GSH.

Protein	k_{cat} (s^{-1})	$K_{M,Hg}$ (μM)	k_{cat}/K_M (M^{-1} s^{-1})
Wild-type	9.0 ± 0.3	16.6 ± 2	5.4 ± 0.3 x 10^5
K99A	0.73 ± 0.03	4.5 ± 1	1.6 ± 0.4 x 10^5
E446Q	0.62 ± 0.03	3.5 ± 0.7	1.8 ± 0.4 x 10^5
K449A	2.4 ± 0.1	2.4 ± 1	1.0 ± 0.4 x 10^6

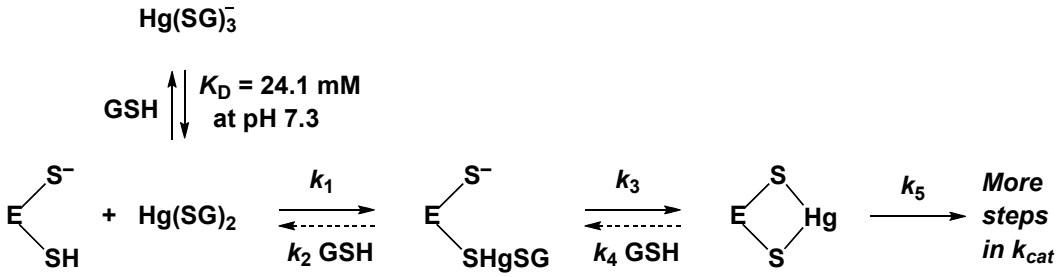

Figure 2.1. Simple two-step CTT mercury acquisition model. This model shows an initial displacement of a glutathione (SG) ligand by a cysteine residue, followed by the displacement of a second glutathione ligand. While three-coordinate complexes do likely exist, they are not depicted here for simplicity.

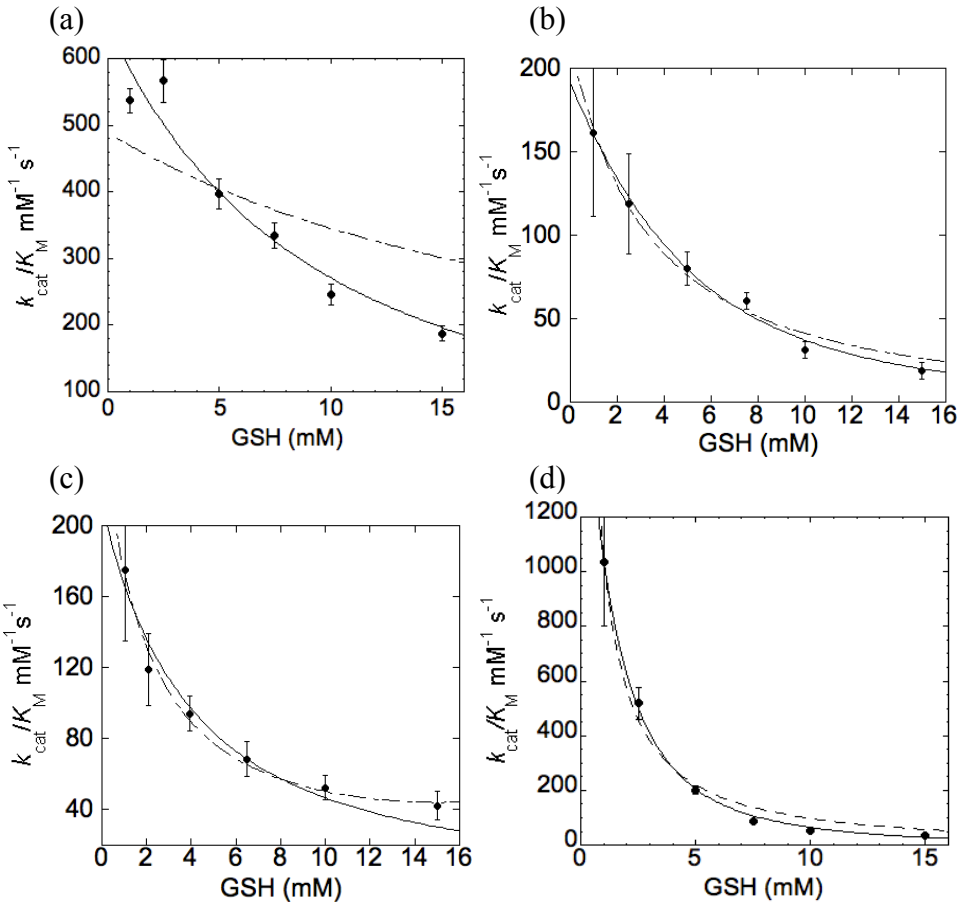

Figure 2.2. Best-fit curves of k_{cat}/K_M vs. [GSH] plots for wild-type (a), K99A (b), E446Q (c), and K449A (d). Wild-type and E446Q data fit best to equation 2.2, while both K99A and K449A fit to equation 2.3, suggesting that both K99A and K449A mutants of MerA result in a more exchangeable pair of C-terminal cysteine residues.

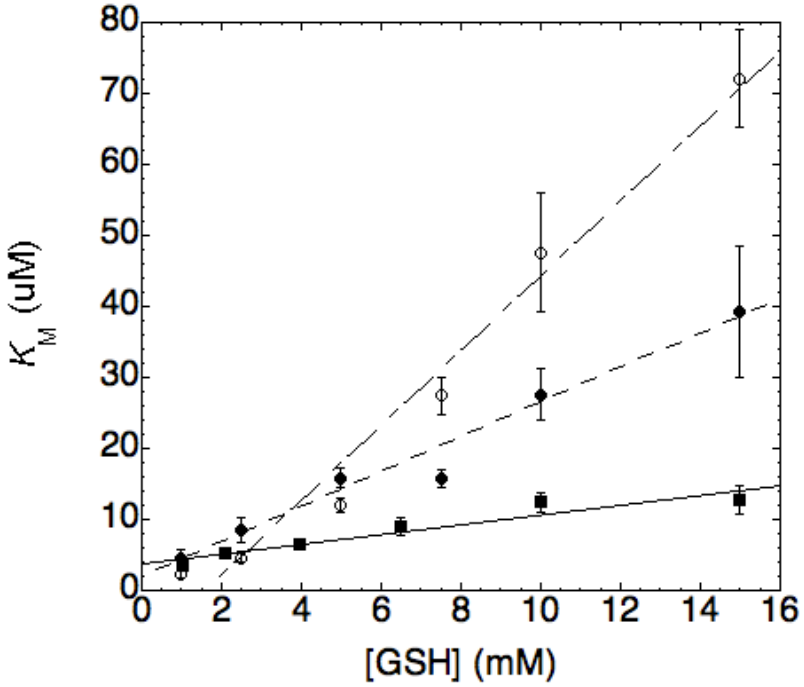

Figure 2.3. Dependence of K_M on [GSH]. The solid line and solid squares are K_M values for E446Q MerA, the evenly dashed line and solid circles are the K_M values for K99A MerA, and the dashed lines and open circles are the K_M values for K449A. The sensitivity of K_M for K99A and K449A MerA is much higher than E446Q MerA.

Table 2.2. Parameters from data fit to equations 2.2 and 2.3 in Figure 2.2.

Protein	k_1 ($mM^{-1} s^{-1}$)	k_2/k_3 (mM^{-1})	k_4/k_5 (mM^{-2})
Wild-type	647 ± 50^{T}	0.068 ± 0.022^{T}	*
K99A	$190 \pm 16^{\Pi}$	$0.13 \pm 0.08^{\Pi}$	$0.1 \pm 0.05^{\Pi}$
E446Q	212 ± 21^{T}	0.22 ± 0.06^{T}	*
K449A	$1982 \pm 374^{\Pi}$	$0.68 \pm 0.35^{\Pi}$	$0.21 \pm 0.14^{\Pi}$

^{T} Fit to equation 2.
$^{\Pi}$ Fit to equation 3.
* Irrelevant parameter.

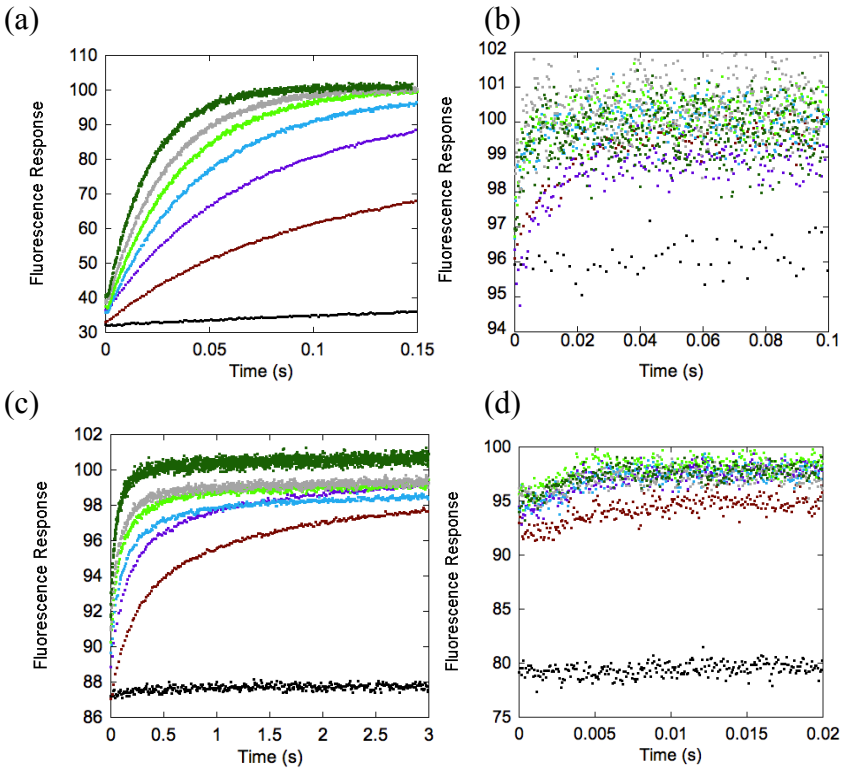

Figure 2.4. Stopped-flow traces from wild-type (a), K99A (b), E446Q (c), and K449A (d). All data fit to double or single exponentials. K99A and K449A MerA data are noisy and resulted in fits with large errors.

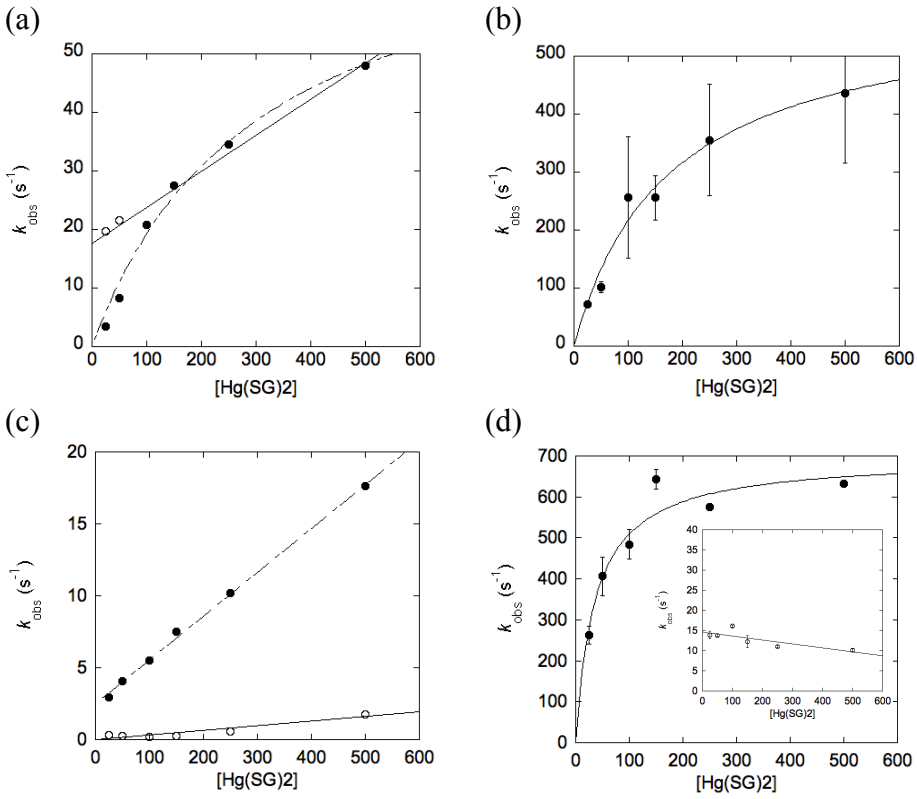

Figure 2.5. Concentration dependence of the observed rate constants for Hg(II) acquisition by wild-type and mutant forms of MerA. The data are arranged with wild-type (a), K99A (b), E446Q (c), K449A (d). Second-order associated observed rate constants are displayed by open circles, while first-order associated observed rate constants are displayed by solid circles. The second rate constant observed for K449A MerA is displayed in the inset, as it was too small compared to the other rate constant. The K99A MerA data fit best to a single exponential.

Table 2.3. Individual rate constants determined from stopped-flow spectrofluorometry data.

Protein	k_1 **(mM^{-1} s^{-1})**	k_2 **(mM^{-1} s^{-1})**	k_3 **(s^{-1})**
Wild-type	256 ± 85	5.30 ± 2.3	78 ± 9
K99A	3408 ± 1217	78.3 ± 53.1	593 ± 65
E446Q	30.5 ± 0.7	*	*
K449A	18900 ± 6500	474 ± 275	697 ± 46

*Cannot be determined due to limitation in available data.

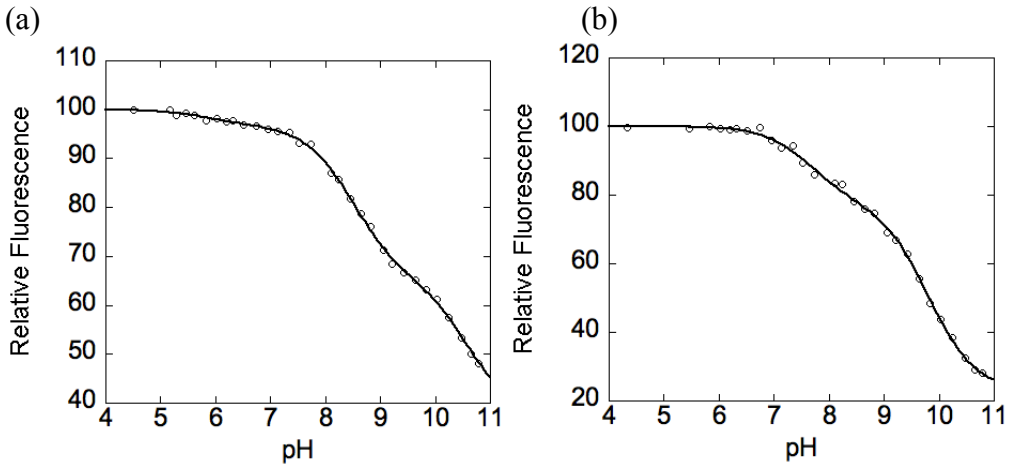

Figure 2.6. Fluorescence pK_a curves. K99A (a) and E446Q (b) MerA are depicted. E446Q MerA only shows two inflection points, while K99A MerA shows three inflection points.

Table 2.4. pK_a values in dimer cleft determined from quenching of the fluorescence of FAD. [Y]

Protein	p$K_{a,1}$	p$K_{a,2}$	p$K_{a,3}$
Wild-Type[9]	*	6.4 ± 0.0	8.8 ± 0.2
K99A	5.9 ± 0.2	8.5 ± 0.0	10.6 ± 0.1
E446Q	*	7.7 ± 0.0	9.8 ± 0.0
K449A	*	8.0 ± 0.0	9.6 ± 0.2

[Y] Data were collected at 25 °C.

[9] Ledwidge et al., JACS 2005.

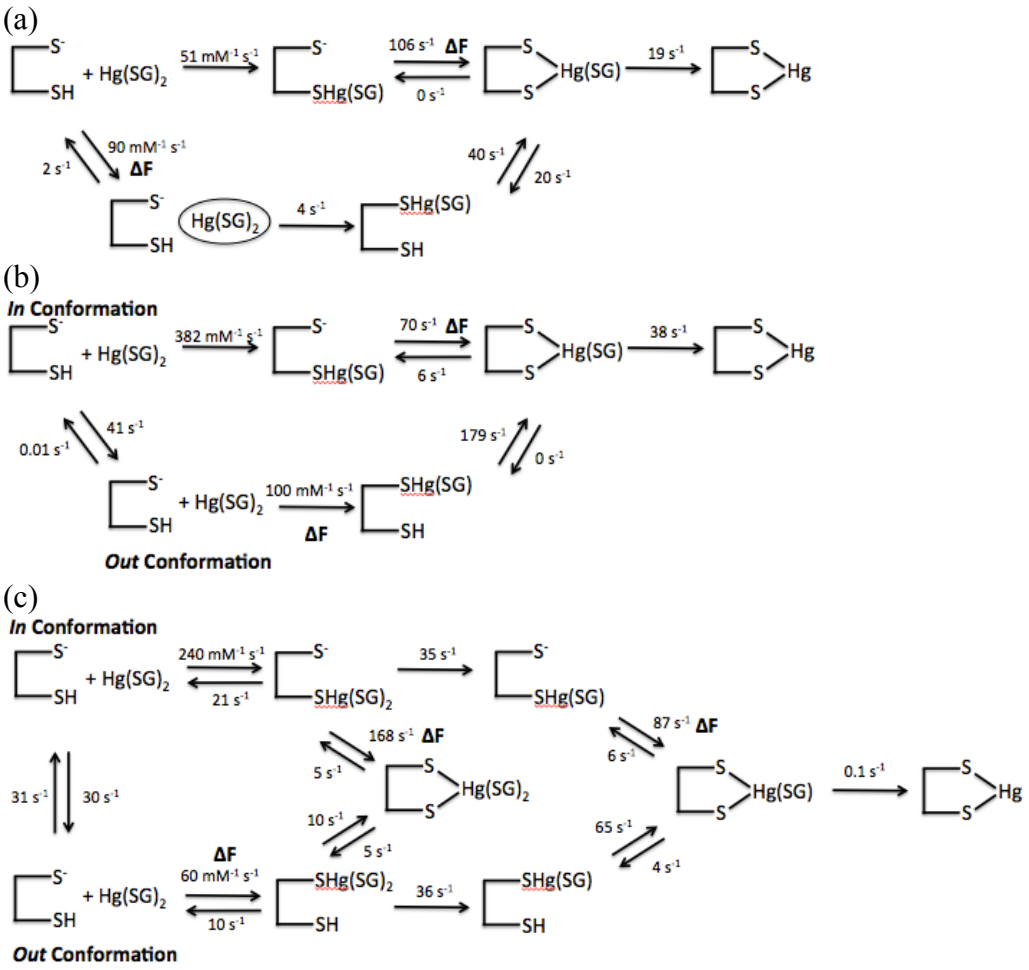

Figure 2.7. Models of Hg(II) acquisition by the CTT of MerA. The two sulfur atoms represent the C-terminal cysteine residues of MerA. The models consist of the pre-binding model (a), CTT equilibrium model (b), CTT equilibrium with 4-coordinate complex model (c).

(a)

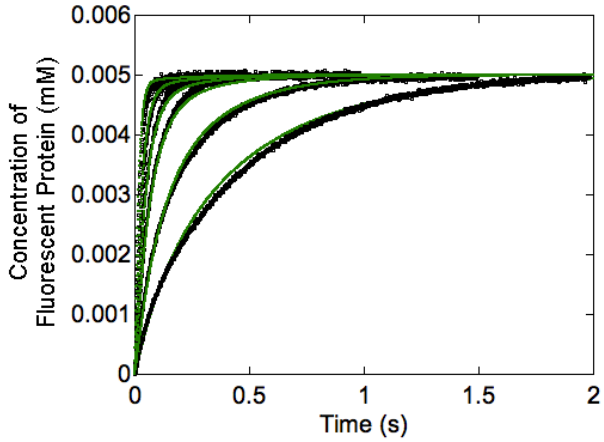

(b)

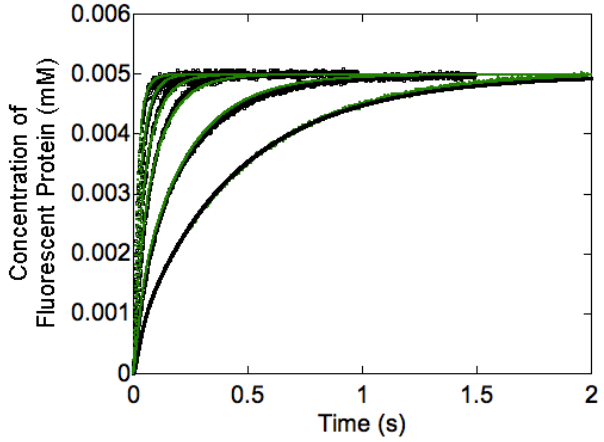

(c)

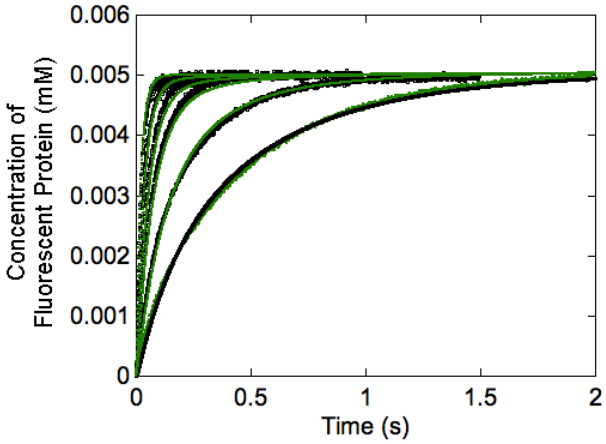

Figure 2.8. Global fit of kinetic models. Figure labels are respective to Figure 2.7. Raw kinetic traces are from wild-type pH 7.3 pre-equilibrium measurements. The raw kinetic traces are in black, and the Berkeley Madonna model traces are in green.

Chapter 3:
Thermodynamics of the MerA Carboxy-terminal Tail

Abstract

We have been making predictions regarding the dynamics of the CTT of MerA using the kinetics of Hg(II) acquisition. As a result, we are slightly limited as to the extent of conclusions we can formulate. The kinetic data for Hg(II) acquisition by the CTT of MerA provided an indirect probe for the states populated by the CTT. To more directly monitor the intrinsic thermodynamics and kinetics of the tail, we utilized nuclear magnetic resonance spectroscopy. The specific goal was to implement CPMG (Carr-Purcell-Meiboom-Gill) (Carr and Purcell, 1954; Meiboom and Gill, 1958), a form of NMR relaxation dispersion that can provide both the fractional populations p_A p_B populated by the CTT and the rate of exchange k_{ex} between the states (Loria et al, 2008).

Isotopic Labeling of MerA

The size of MerA – a dimer consisting of 50 kDa monomers – is quite large and not highly adaptable to NMR, where 30 kDa proteins are typically the upper limit, but we have seen applications of NMR to increasingly large protein complexes (Sprangers et al., 2005). Large proteins pose two issues regarding their experimentation with NMR: (1) a large protein results in a large number of resonances, of which many will overlap, and (2) the rotational correlation time τ_c of large proteins is high, resulting in broadened resonances that may not be

observable (Kleckner and Foster, 2011). This is demonstrated in the preliminary ^{15}N-^{1}H HSQC spectrum obtained for wild-type MerA (Figure 3.1).

While the initial ^{15}N-^{1}H HSQC spectrum of wild-type MerA showed some individual resonances, the vast majority overlap with at least one other resonance. While that doesn't preclude the presence of at least one effective probe for the dynamics of the CTT, it highly limits the probability of obtaining useful information from these spectra. Fortunately, there exists greater flexibility within parts of the protein, which prevent at least some of the resonances from being completely broadened out (Kleckner and Foster, 2011). This suggests that limiting the number of resonances in the spectrum of MerA may be effective in producing more individual resonances to investigate as probes for the dynamics of the CTT.

To limit the number of resonances in the NMR spectra in hopes of decreasing the overlap of resonances, we specifically ^{13}C-labeled methyl groups of isoleucine, leucine, and valine (ILV) in MerA. Unfortunately, still 80 % of the resonances in the ILV-labeled protein overlapped (Figure 3.2). The Ile portion of the spectrum showed the least overlap, and many of the existing individual resonances had higher intensities.

CTT-Sensitive NMR probes

We determined if any of the resonances we observed in the ^{13}C-^{1}H HSQC were sensitive to the CTT by creating a Δ10 MerA mutant that is missing the last 10 residues of the CTT. We assumed that with the tail of MerA removed,

resonances that were affected by the electrical environment of the tail would show either a chemical shift difference or intensity difference, where an intensity difference would suggest a change in the dynamics of the tail.

The ILV-labeled ^{13}C-^{1}H HSQC spectrum of this mutant is overlaid with the wild-type MerA spectrum in Figure 3.3. Given the limited number of individually resolved resonances, we were surprised to be able to locate at least a few resolved resonances that showed real differences between the two proteins, suggesting that they could work as potential probes for the dynamics of the CTT.

The majority of the changes in the resonances involved chemical shift differences. One of the resonances in the Ile portion of the spectrum did disappear between the wild-type and Δ10 MerA. Since there were no Ile residues in the CTT, we suspect that the resonance was broadened out, which lowered its detectability. There may have been losses of resonances or changes in chemical shifts in the Val and Leu region of the spectrum; however, many of them were likely located in the middle region of largely overlapping resonances.

With the potential that we had individually resolved resonances that could be probes for the MerA CTT dynamics, we proceeded to assigning the resonances to a subset of the residues within the protein.

Isolating and Assigning Effective Probes of the CTT Dynamics

Since optimizing the NMR spectra of a large protein beyond a certain resolution is difficult, especially labeling the protein, we endeavored to at least determine which resonances within the ILV spectrum of MerA correlated with

which residues within the protein, as opposed to assigning a residue to each resonance.

Using proximity to the CTT as a metric for the relevance of a residue as a probe for the dynamics of the CTT, we were able to find a subset of the labeled residues that would be relevant NMR probes. To further subdivide the relevant probes, we only considered the isoleucine residues, as this portion of the HSQC spectrum for wild-type ILV-labeled MerA was the most resolved. From these, three residues remained. These residues consisted of I38, I103 and I329. As I103 is the closest of these residues to the CTT (Figure 3.4), we proposed that this residue might act as a good NMR probe of the CTT dynamics.

To determine which of the resonances in the Ile-portion of the HSQC spectrum was associated with I103, we mutated this residue to valine, and only ^{13}-C methyl labeled the isoleucine residues. The resulting HSQC spectrum was overlaid on the HSQC spectrum of wild-type MerA (Figure 3.5). The evident disappearance of the resonance at 8 ppm ^{13}C and 0.6 ppm ^{1}H is most likely associated with the I103 residue.

The characteristics of this resonance are not promising in terms of utilizing it as a probe for CPMG experiments. Primarily, the sharp intensity of the resonance suggests the residue is in the fast exchange regime ($k_{ex} > \Delta\omega$), as seen in Figure 3.5. For CPMG experiments, the resonance must be in an intermediate exchange regime ($k_{ex} \approx \Delta\omega$), which provides an enhanced transverse relaxation rate R_{ex} ($R_{2,obs} = R_{2,i}+R_{ex}$), where R_{ex} represents the underlying dynamics of the protein (Palmer et al., 2001).

Further analysis of the HSQC spectra reveal that most of the resonances are not amenable to CPMG experiments, preventing further work pursuing the dynamics of the MerA CTT. While there appear to be Ile resonances in the Val and Leu regions of the spectra in Figure 3.5, these resonances are likely not Ile-associated resonances. Goto et al in 1999 were able to show that [3,3-$^{2}H_2$] α-ketobutyrate is primarily metabolized into isoleucine and [3-^{2}H] α-ketoisovalerate is primarily metabolized into valine and leucine; however, since the metabolic pathways for these residues use some of the same enzymes, and the residues act as regulators of the enzymes, scrambling of the metabolites between different catabolic pathways can occur, particularly at higher concentrations of the precursors. Consequently, the additional resonances observed are not rogue, individually resolved resonances that can be assigned and utilized as NMR probes for the CTT dynamics, but rather they are ^{13}C-methyl groups that have been incorporated into other valine and leucine residues.

NMR Conclusions

Significant improvements in the resolution of the resonances in the HSQC spectra were obtained through ^{13}C-methyl ILV labeling. This provided a more interpretable ^{13}C-^{1}H HSQC spectrum compared to the ^{15}N-^{1}H HSQC spectrum. In fact, we were even able to isolate a set of resonances that indicated sensitivity to the tail dynamics (Figure 3.3).

A rational approach to labeling resonances that appeared to show sensitivity to the tail dynamics provided an intense peak that could have been

used as an NMR probe. Unfortunately, the labeled resonance was in too fast of an exchange regime to be utilized in CPMG experiments.

A simple NMR experiment involving the use of a series of mutations in the ionic triad residues that would be predicted to induce increasing flexibility in the tail may be used in conjunction with the high intensity resonance associated with I103 to perform a pseudo-titration that may reveal a K_d for the tail. While full characterization of populations and rates of the CTT in MerA seem to elude elucidation, other labeling techniques could reduce the number of irrelevant resonances, which would de-convolute the spectrum. One example is reductive alkylation of lysine residues (Hattori et al., 2013). This would provide a probe on all lysine residues, including K99 and K449. Unfortunately, this would only provide a relevant probe of the CTT dynamics in the case where the tail is presumed to be more liberated, as the addition of the methyl group to the lysine would be believed to disrupt the CTT-lysine interactions. Given the number of NMR techniques available and the rate of method development, a relevant technique will become available to fully characterize the CTT rates and states.

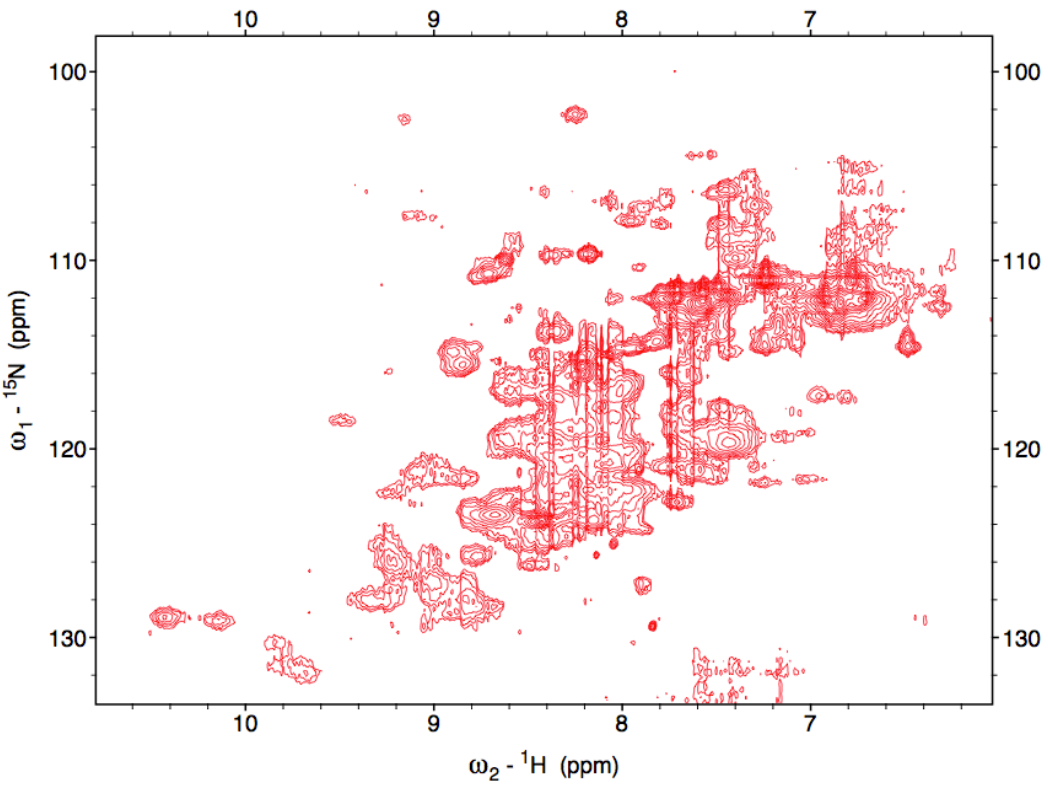

Figure 3.1. ^{15}N-^{1}H HSQC of wild-type MerA. Only a small set of the resonances are clearly resolved. Most of the resonances have either overlapped with nearby resonances or are broadened beyond detectability. In either case, the spectrum remains interpretable.

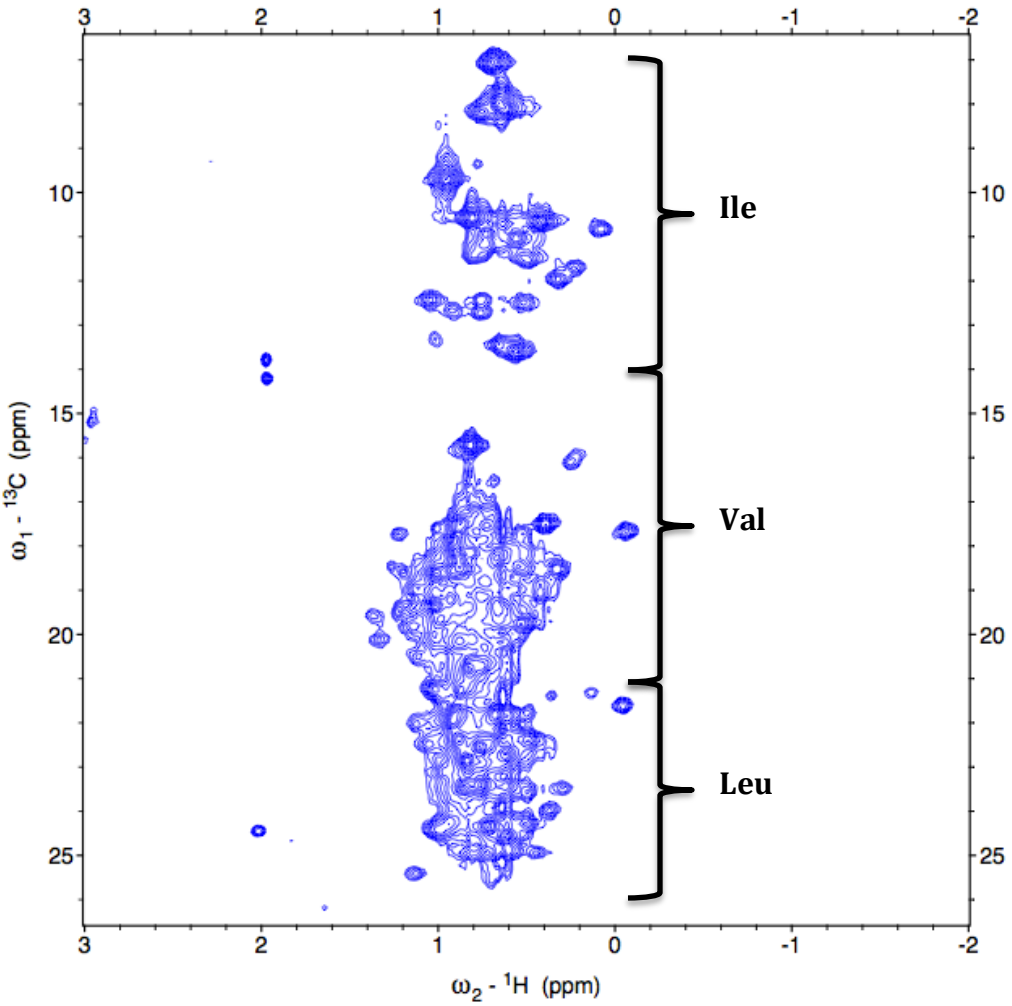

Figure 3.2. ^{13}C-^{1}H HSQC of MerA with ^{13}C-methyl labeling on isoleucine, leucine and valine. While the spectrum is still quite crowded with resonances, there exist enough fully resolved resonances to find at least one probe for the CTT dynamics. The isoleucine region of the spectrum showed the greatest resolution.

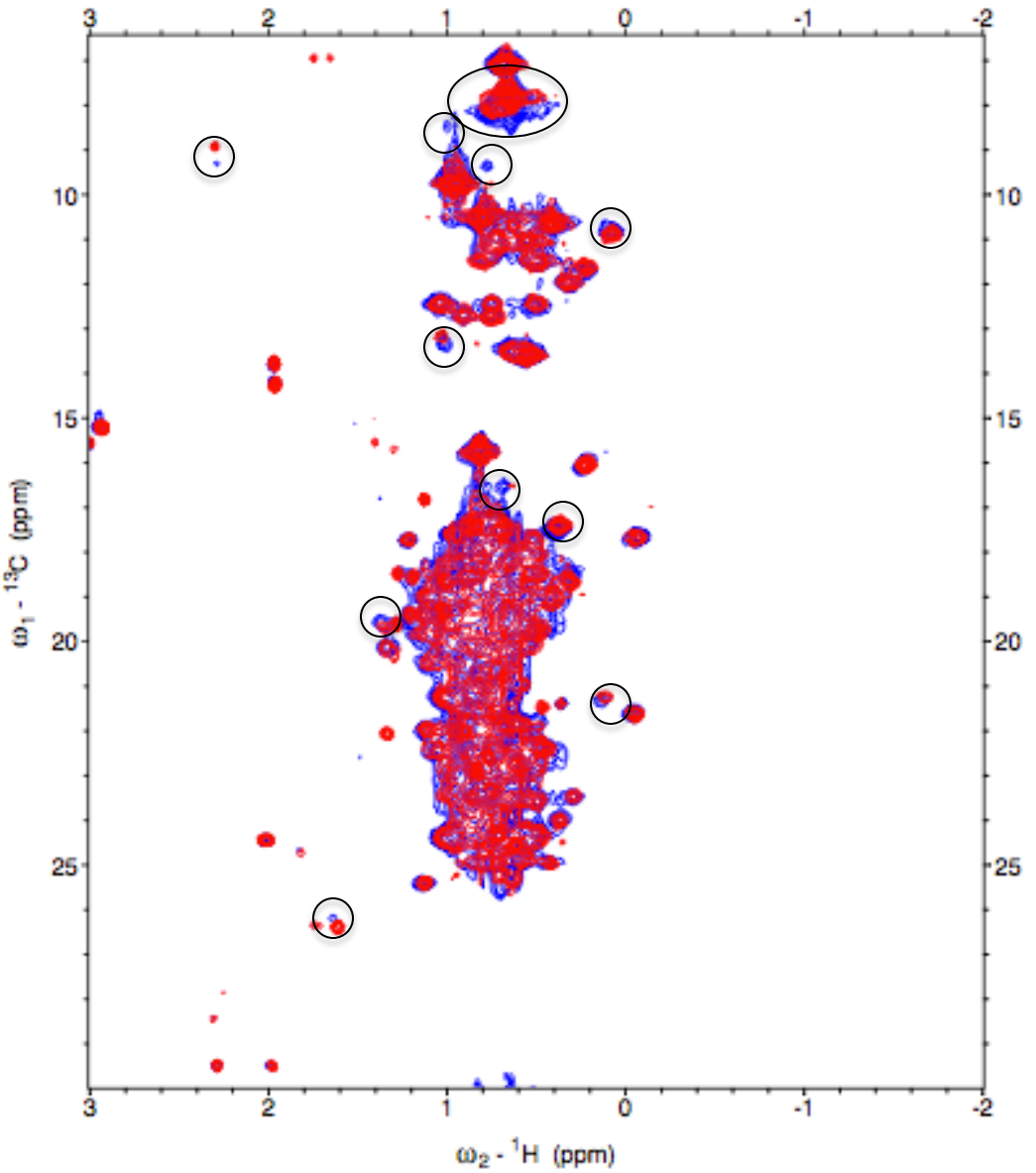

Figure 3.3. Overlay of the wild-type and Δ10 MerA ^{13}C-^{1}H HSQC. Wild-type protein is in blue, while the Δ10 mutant is in red. Some chemical shift differences can be observed, particularly in the ILE region of the spectrum (black circles).

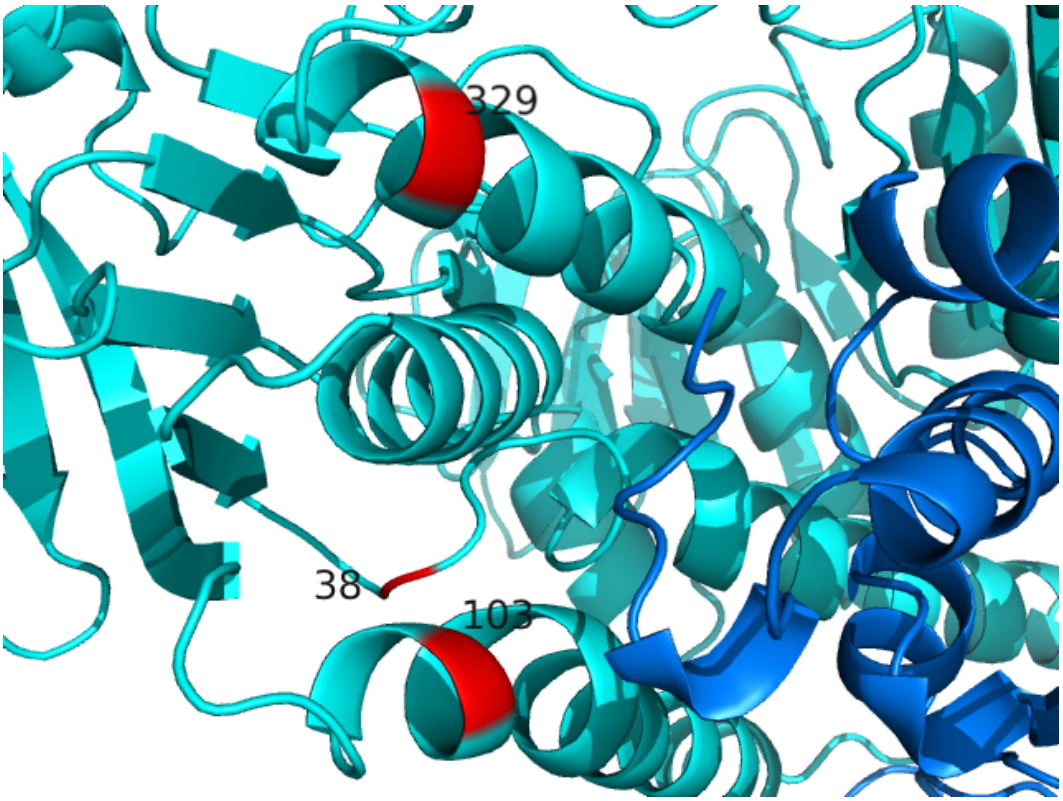

Figure 3.4. Relevant isoleucine NMR probes for the MerA CTT dynamics. Isoleucine residues in the vicinity of the CTT in the dimer cleft are located on the red regions of the cartoon structure. The number of the residue in the sequence appears near the highlighted region. As is evident by the structure, I103 is located closest to the CTT.

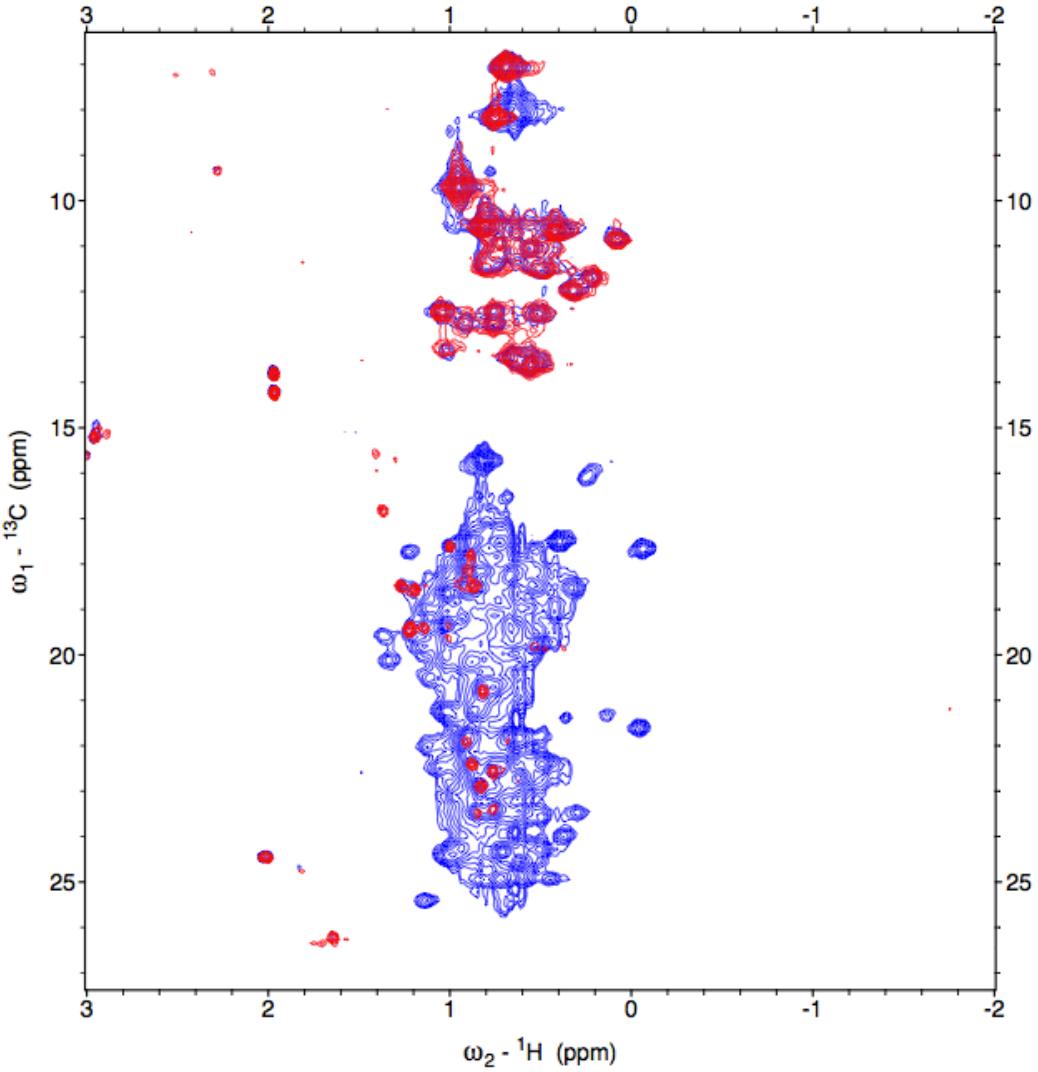

Figure 3.5. ^{13}C-^{1}H HSQC spectra of wild-type ILV-labeled and I103V ^{13}C-Isoleucine-labeled MerA. Wild-type protein is depicted in blue, while the I103V protein is depicted in red. The location of the I103-associated resonance is at 8 ppm ^{13}C and 0.6 ppm ^{1}H, which is evidenced by the disappearance of the resonance in the I103V MerA spectrum.

Chapter 4:
The Flexibility of Carboxy-terminal Tails

Conclusions

In previous chapters we have argued that the C-terminal tail of MerA plays a significant role in the overall kinetics of Hg(II) acquisition and reduction to Hg(0). It has also been argued that there is a necessary, well-balanced equilibrium of the CTT between an *in* and *out* conformation that allows for efficient delivery of Hg(II) into the inner cysteine pair. In fact, steady-state data revealed that mutations that are believed to disrupt this equilibrium also drastically decrease k_{cat}, which is significant since the transport of Hg(II) to the catalytic cysteine residues is not the rate limiting step in wild-type enzyme and has now overcome the slow rate of reduction of Hg(II) and release of NADP+ to become the rate limiting step.

Our data strongly suggest that a set of highly conserved, electrostatic residues within the dimer cleft of MerA act to modulate the CTT intrinsic dynamics to maintain both the *in* and *out* populations that allow MerA to acquire Hg(II) from the *out* conformation and release Hg(II) from the *in* conformation. These residues were determined to be K99, E446, and K449 in the Tn*501* MerA catalytic core.

Both pre-equilibrium and steady-state data supported the role of the lysine residues to stabilize the tail in the dimer cleft as the *in* conformation and the glutamate residue to oppose significant stabilization of the CTT in the dimer cleft to favor the *out* conformation. For the K99A and K449A mutations, pre-equilibrium in conjunction with steady-state data showed substantial increases in

k_1, k_2, and k_3 from the scheme in Figure 2.1. Likewise, the E446Q mutation showed a decrease in k_1, k_2, and k_3 from the scheme in Figure 2.1. These kinetic data strongly suggested the previously prescribed roles of these residues. Additionally, the sensitivity of the K_M for the K99A and K449A mutations was much higher than the E446Q mutation, suggesting that the tail was more exposed to bulk solvent in the lysine mutants, which allowed for greater accessibility of GSH to the CTT-bound Hg(II).

While we did not obtain any NMR relaxation dispersion data in this body of work, we are confident the populations and rates derived from CPMG experiments probing the dynamics of the CTT would have provided evidence supporting our kinetic data that revealed the roles of K99, E446, and K449. We also believe, relaxation dispersion data would have augmented our argument that the CTT dynamics are intrinsic, and the tail dynamics are not driven by the presence or absence of bound Hg(II) on the CTT.

Since we cannot parse the kinetic data to reveal dynamic effects from chemical kinetic effects, especially from steady-state data, relaxation dispersion data would have helped us differentiate between changes in k_{cat} and k_{cat}/K_M that were related to dynamics or changes in chemical kinetics. Fortunately, pre-equilibrium kinetic data reflected pure CTT acquisition rates without complications from the reduction steps of the reaction; however, we cannot rule out the role that the lysine residues played in modulating the pK_a values of the C-terminal cysteine residues, which likely would have effected Hg(II) acquisition rates as well.

It is difficult to confidently expand our results revealing the effects of the ionic triad residues on the CTT of MerA to other proteins with CTTs, such as the TrxR/glutaredoxin fusion protein and ribonucleotide reductase, since previous studies on TrxR revealed a set of residues consisting of two asparagine residues and a tryptophan residue, termed the guiding bar residues, that were believed to at least stabilize the CTT on the protein so as to decrease conformational entropy of the tail (Fritz-Wolf et al., 2007). We found two lysine residues and a glutamate residue that acted to stabilize and destabilize, respectively, the CTT in the dimer cleft. There is no significant relationship between the ionic triad residues and the guiding bar residues in terms of interaction types. To begin to define a common mechanism for modulating CTT dynamics, additional work would need to be completed in probing the residues effecting the TrxR/glutaredoxin fusion and ribonucleotide reductase. We can at least conclude that these proteins must have evolved with residues that are necessary for controlling the protein-tail flexibility.

Our work here represents progress toward fully elucidating the conserved residues involved in the acquisition and reduction of Hg(II) in MerA. This alone may contribute toward optimizing applications in the phytoremediation of Hg(II) or MeHg(I) contaminated soils. While still a distant dream, given our inability to *de novo* design efficient enzymes, even with the assistance of existing protein scaffolds and the use of directed evolution (Siegel et al., 2010), the ultimate goal would be to have protein C-terminal tails incorporated into the design features of proteins, particularly oxidoreductase enzymes that could have industrial applications in the future. At least for now, we will settle with the recognition

that this work advances our basic understanding of enzyme structure and function, which alone represents an important step toward translating basic research into applied science with economic and civil societal impact.

Bibliography

Aglietti RA, Floor SN, McClendon CL, Jacobson MP, Gross JD. Active site conformational dynamics are coupled to catalysis in the mRNA decapping enzyme Dcp2. Structure. 2013;21:1571-1580.

Altschul SG, Gish W, Miller W, Myers EW, Lipman DJ. Basic local alignment search tool. J Mol Biol. 1990;215:403-410.

AMAP/UNEP. Technical Background Report to the Global Atmospheric Mercury Assessment. Arctic Monitoring and Assessment Programme/UNEP Chemicals Branch; 2008. p 159

Ansari AZ, Chael ML, O'Halloran TV. Allosteric underwinding of DNA is a critical step in positive control of transcription by Hg-MerR. Nature. 1991;355, 87-89.

Ansari AZ, Bradner JE, O'Halloran TV. DNA-bend modulation in a repressor-to-activator switching mechanism. Nature. 1995;374:371-375.

Barkay T, Miller SM, Summers AO. Bacterial mercury resistance from atoms to ecosystems. FEMS Microbiol Rev. 2003;27:355-384.

Begley TP, Walts AE, Walsh CT. Bacterial organomercurial lyase: overproduction, isolation, and characterization. Biochemistry. 1986;25:7186-7192.

Brown NL, Ford SJ, Pridmore RD, Fritzinger DC. Nucleotide sequence of a gene from the *Pseudomonas* transposon Tn*501* encoding mercuric reductase. Biochemistry. 1983;22:4089-4095.

Brown NL, Pridmore RD, Fritzinger DC. The mercury-resistance genes of transposon Tn*501* – nucleotide sequence of the *mer* operon and a possible mechanism for mercury detoxification. Biochem Soc Trans. 1984;12:276-277.

Brown NL, Misra TK, Winnie JN, Schmidt A, Seiff M, Silver S. The nucleotide sequence of the mercuric resistance operons of plasmid R100 and transposon Tn*501* – further evidence for *mer* genes which enchance the activity of the mercuric ion detoxification system. Mol Gen Genet. 1986; 202:143-151.

Brown NL, Stoyanov JV, Kidd SP, Hobman JL. The MerR family of transcriptional regulators. FEMS Microbiol Rev. 2003;27:145-163.

Barrineau P, Gilbert P, Jackson WJ, Jones CS, Summers AO, Wisdon S. The DNA sequence of the mercury resistance operon of the IncFII plasmid NR1. J Mol Appl Genet. 1984;2:601-619.

Barrineau P, Gilbert P, Jackson WJ, Jones CS, Summers AO, Wisdom S. The structure of the *mer* operon. Basic Life Sci. 1985;30:707-718.

Carr HY, Purcell EM. Effects of diffusion on free precession in nuclear magnetic resonance experiments. Phys Rev. 1954;94:630.

Chakraborty LB, Qureshi A, Vadenbo C, Hellweg S. Anthropogenic mercury flows in India and impacts of emission controls. Environ Sci Technol. 2013;47:8105-8113.

Cheesman BV, Arnold AP, Rabenstein DL. Nuclear magnetic resonance studies of the solution chemistry of metal complexes. 25. $Hg(thiol)_2$ complexes and Hg(II)-thiol ligand exchange kinetics. J Am Chem Soc. 1988;110:6359-6364.

Clarkson TW, Magos L. The toxicology of mercury and its chemical compounds. Crit Rev Toxicol. 2006;36:609-662.

Crawley SW, Gharaei MS, YE Q, Yang Y, Raveh B, London N, Schueler-Furman O, Jia Z, Cote GP. Autophophorylation activates *Dictyostelium* myosin II heavy chain kinase A by providing a ligand for allosteric binding site in the α-kinase domain. 2010;286:2606-2616.

Delaglio F, Grzesiek S, Vuister GW, Zhu G, Pfeifer J, Bax A. NMRPipe: a multidimensional spectral processing system based on Unix pipes. J Biomol NMR 1994;6:277-293.

Doucleff M, Terry N. Pumping out the arsenic. Nat Biotechnol. 2002;20:1094-1095.

Eisenmesser EZ, Millet O, Labeikovsky W, Korzhnev DM, Wolf-Watz M, Bosco DA, Skalicky JJ, Kay LE, Kern D. Intrinsic dynamics of an enzyme underlies catalysis. Nature Letters 2005;438:117-121.

Engst S, Millers SM. Rapid reduction of Hg(II) by mercuric ion reductase does not require the conserved C-terminal cysteine pair using $Hg(Br)_2$ as the substrate. Biochemistry. 1998;37:11496-11507.

Engst S, Miller SM. Alternative routes for entry of HgX_2 into the active site of mercuric ion reductase depend on the nature of the X ligands. Biochemistry. 1999;38:3519-3529.

Foster TJ. Plasmid-determined resistance to antimicrobial drugs and toxic metal ions in bacteria. Microbiol. Rev. 1983;47:361-409.

Furukawa K, Tonomura K. Enzyme system involved in the decomposition of phenyl mercuric acetate by mercury-resistant *Pseudomonas* K-62. Agric Biol Chem. 1971;35:604-610.

Furukawa K, Tonomura K. Metallic mercury releasing enzyme in mercury-resistant *Pseudomonas*. Agric Biol Chem. 1972;36:217-226.

Fox BS, Walsh CT. Mercuric reductase. Purification and characterization of a transposon-encoded flavoprotein containing an oxidation-reduction-active disulfide. Biochemistry 1982;257:2498-2503.

Fritz-wolf K, Urig S, Becker K. The structure of human thioredoxin reductase 1 provides insights into C-terminal rearrangements during catalysis. J Mol Biol. 2007;370:116-127.

Goto NK, Gardner KH, Mueller GA, Willis RC, Kay LE. A robust and cost-effective method for the production of Val, Leu, Ile (δ1) methyl-protonated ^{15}N-, ^{13}C, ^{2}H-labeled proteins. J Biomol NMR. 1999;13:369-374.

Gray JE, Hines ME. Mercury: distribution, transport, and geochemical and micro-bial transformations from natural and anthropogenic sources. Appl Geochem. 2006;21:1819-1820.

Gustin MS, Lindber SE, Weisber PJ. An update on the natural sources and sinks of atmospheric mercury. Appl Geochem. 2008;23:482-493.
Hamlett NV, Landale EC, Davis BH, Summers AO. Roles of the Tn*21* *merT*, *merP*, and *merC* gene products in mercury resitance and mercury binding. J Bacteriol. 1992;174:6377-6385.
Harada M. Minamata disease: methylmercury poisoning in Japan caused by environmental pollution. Crit Rev Toxicol. 1995;25:1-24.
Hattori Y, Furuita K, Ohki I, Ikegami T, Fukada H, Shirakawa M, Fujiwara T, Kojima C. Utilization of lysine ^{13}C-methylation NMR for protein-protein interaction studies. J Biomol NMR. 2013;55:19-31.
Heltzel A, Lee IW, Totis PA, Summers AO. Activator-dependent preinduction binding of sigma-70 RNA polymerase at the metal-regulated *mer* promoter. Biochemistry. 1990;29:9572-9584.
Hilson G, Hilson CJ, Pardie S. Improving awareness of mercury pollution in small-scale gold mining communities: Challenges and ways forward in rural Ghana. Environ Resear. 2007;103:275-287.
Hong B, Nauss R, Harwood IM, Miller SM. Direct Measurement of Mercury(II) Removal from Organomercurial Lyase (MerB) by Tryptophan Fluorescence: NmerA Domain of Coevolved γ-Proteobacterial Mercuric Ion Reductase (MerA) Is More Efficient Than MerA Catalytic Core or Glutathione. Biochemistry. 2010;49:8187-8196.
Huang HH, Day L, Cass CL, Ballou DP, Williams CH Jr, Williams DL. Investigations of the catalytic mechanism of thioredoxin reductase from *Schistosoma mansoni*. Biochemistry. 2011;50:5870-5882.
Inoue K. Heavy Metal Toxicity. J Clinic Toxicol. 2013;S3:007.
Jackson WJ, Summer AO. Biochemical characterization of the $HgCl_2$-inducible polypeptides encoded by the *mer* operon of plasmid R100. J Bacteriol. 1982;151:962-970.
Johs A, Harwood IM, Parks JM, Nauss RE, Smith JC, Liang L, Miller SM. Structural characterization of intramolecular Hg^{2+} transfer between flexibly linked domains of mercuric ion reductase. J Mol Biol. 2011;413:639-656.
Kang-Yum E, Oransky SH. Chinese patent medicine as a potential source of mercury poisoning. Vet Hum Toxicol. 1992;34:235-238.
Kay LE, Keifer P, Saarinen T. Pure absorption gradient enhanced heteronuclear single quantum correlation spectroscopy with improved sensitivity. J Am Chem Soc. 1992;114:10663-10665.
Kleckner IR, Foster MP. An introduction to NMR-based approaches for measuring protein dynamics. Biochim et Biophys Acta. 2011;1814:942-968.
Kleiger G, Saha A, Lewis S, Kuhlman B, Deshaies RJ. Rapid E2-E3 assembly and disassembly enable processive ubiquitylation of cullin-RING ubiquitin ligase substrates. Cell. 2009;139:957-968.

Kramers HA. Brownian motion in a field of force and the diffusion model of chemical reactions. Physica. 1940;7:284-304.
Kramers U. Phytoremediation: novel approaches to cleaning up polluted soils. Curr Opin Biotechnol. 2005;16:133-141.
Kulkarni R, Summers AO. MerR crosslinks to the α, β, σ^{70} subunits of RNA polymerase in the preinitiation complex at the *merTPCAD* promoter. Biochemistry. 1999;38,3362-3368.
Lafrance-Vanasse J, Lefebvre M, Di Lello P, Sygusch J, Omichinski JG. Crystal structures of the organomercurial lyase MerB in its free and mercury-bound forms: insights into the mechanism of methylmercury degradation. J Biol Chem. 2009;284:938-944.
Lamborg CH, Fitzgerald WF, O'Donnell J, Torgersen T. A non-steady-state compartmental model of global-scale mercury biogeochemistry with interhemispheric atmospheric gradients. Geochim Cosmochim Acta. 2002;66:1105-1118.
Larkin MA, Blackshields G, Brown NP, Chenna R, McGettigan PA, McWilliam H, Valentin F, Wallace IM, Wilm A, Lopez R, Thompson JD, Gibson TJ, Higgins DG. Clustal W and Clustal X version 2.0. Bioinformatics. 2007;23:2947-2948.
Ledwidge R, Patel B, Dong A, Fiedler D, Falkowski M, Zelikova J, Summers AO, Pai EF, Miller SM. NmerA, the metal binding domain of mercuric ion reductase, removes Hg2+ from proteins, delivers it to the catalytic core, and protects cells under glutathione-depleted conditions. Biochemistry 2005;44:11402-11416.
Ledwidge R., Soinski R. Miller SM. Direct monitoring of metal ion transfer between two trafficking proteins. J Am Chem Soc. 2005;127:10842-10843.
Lindqvist O. et al. Mercury in the Swedish environment. Water Air Soil Pollut. 1991;55:23-30.
Loria JP, Berlow RB, Watt ED. Characterization of enzyme motions by solution NMR relaxation dispersion. Acc Chem Res. 2008;41:214-221.
Lund PA, Fod SJ, Brown NJ. Transcriptional regulation of the mercury resistance genes of transposon Tn*501*. J Gen Microbiol. 1986;132:465-480.
Lund PA, Brown NL. Role of the *merT* and *merP* gene products of transposon Tn*501* in the induction and expression of resistance to mercuric ions. Gene. 1987;52:207-214.
Lund PA, Brown NL. Regulation of transcription in *Escherichia coli* from the *mer* and *mer*R promoters in the transposon Tn*501*. J. Mol. Biol. 1989;205:343-353.
Manson RP, Fitzgerald WF, Morel FMM. The bio-geochemical cycling of elemental mercury: anthropogenic influences. Geochim Cosmochim Acta. 1994;58:3191-3198.

Meiboom S, Gill D. Modified spin-echo method for measuring nuclear relaxation times. Rev Sci Instrum. 1958;29:688.
Moore MJ, Walsh CT. Mutagenesis of the N- and C-terminal cysteine pairs of Tn*501* mercuric ion reductase: consequences for bacterial detoxification of mercurial. Biochemistry. 1989;28:1183-1194.
Munthe J. The aquesous oxidation of elemental mercury by ozone. Atmos Environ. 1992;26A:1461-1468.
Munthe J., McElroy W. J. Some aquesous reactions of potential importance in the atmospheric chemistry of mercury. Atmos Environ. 1992;26A:553-556
Munthe J., Xiao Z. F., Lindqvist O. The aqueous reduction of divalent mercury by sulfite. Water Air Soil Pollut. 1991;56:621-630.
Nashine VC, Hammes-Schiffer S, Benkovic S. Coupled motions in enzyme catalysis. Curr Opin Chem Biol. 2010;14:644-651.
Nriagu J. O. A global assessment of natural sources of atmospheric trace metals. Nature. 1989;338:47-49.
Palmer AG, Kroenke CD, Loria JP. Nuclear magnetic resonance methods for quantifying microsecond-to-millisecond motions in biological macromolecules. Methods Enzymol. 2001;339:204-238.
Parks JM, Guo H, Momany C, Liang L, Miller SM, Summers AO, Smith JC. Mechanism of Hg-C protonolysis in the organomercurial lyase MerB. J Am Chem Soc. 2009; 131:13278-13285.
Rasmussen PE. Current methods of estimating atmospheric mercury fluxes in remote areas. Environ Sci Technol. 1994;28:2233-2241.
Robinson JB, Touvinen OH. Mechanisms of microbial resistance and detoxification of mercury and organomercury compounds: physiological, biochemical, and genetic analyses. Microbiol Rev. 1984;48:95-124.
Ruiz RN and Daniell H. Genetic engineering to enhance mercury phytoremediation. Curr Opin Biotechnol. 2009;20:213-219.
Sahlman L, Wong W, Powlowski J. A mercuric ion uptake role for the integral inner membrane protein, MerC, involved in bacterial mercuric ion resistance. J Biol Chem. 1997;272:29518-29526.
Salt DE, Smith RD, Raskin I. Phytoremediation. Annu Rev Plant Physiol Plant Mol Biol. 1998;49:643-668.
Schiering N, Kabsch W, Moore MJ, Distefano MD, Walsh CT, Pai EF. Structure of the detoxification catalyst mercuric ion reductase from *Bacillus* sp. Strain RC607. Nature. 1991;352:168-172.
Schroeder WH, Munthe J. Atmonspheric Mercury – An Overview. Atmosp Environ. 1997;32:809-822.
Shukla GS, Singhal RL. The present status of biological effects of toxic metals in the environment: lead, cadmium, and manganese. Can J Physiol Pharmacol. 1984;62:1015-1031.
Siegel JB, Zanghellini A, Lovick HM, Kiss G, Lambert AR, St Clair JL, Gallaher JL, Hilvert D, Gelb MH, Stoddard BL, Houk KN, Michael FE, Baker D. Computational design of an enzyme catalyst

for a stereoselective biomolecular Diels-Alder reaction. Science. 2010;329:309-313.
Sprangers R, Gribun A, Hwang PM, Houry WA, Kay LE. Quantitative NMR spectroscopy of supramolecular complexes: dynamic side pores in ClpP are important for product release. PNAS. 2005;102:16678-16683.
Steele RA, Opella SJ. Structures of the reduced and mercury bound-forms of MerP, the periplasmic protein from the bacterial mercury detoxification system. Biochemistry. 1997;36:6885-6895.
UNEP Chemical Branch. The global atmospheric mercury assessment: sources, emissions and transport. Geneva: UNEP-Chemicals Branch; 2008. p 44.
Vallee BL and Ulmer DD. Biochemical effects of mercury, cadmium, and lead. Annu Rev Biochem. 1972;41:91-128.
Wilson JR, Leang C, Morby AP, Hobman JL, Brown NL. MerF is a mercury transport protein: different structures but a common mechanism for mercuric ion transporters? FEBS Lett. 2000;471:78-82.
Zahir F, Rizwi SJ, Haq SK, Khan RH. Low dose mercury toxicity and human health. Environmental Toxicology and Pharmacology. 2005;20:351-360.
Zeng Q, Stalhandske C, Anderson MC, Scott RA, Summers AO. The core metal recognition domain of MerR. Biochemistry. 1998;37:15885-15895.
Zhang Y, An X, Stubbe J, Huang M. Investigation of in vivo roles of the C-terinal tails of small subunit (ββ') of *Saccharomyces cerevisiae* ribonucleotide reductase: contribution to cofactor formation and intersubunit association within the active holoenzyme. J Biol Chem. 2013;288:13951-13959.

Publishing Agreement

It is the policy of the University to encourage the distribution of all theses, dissertations, and manuscripts. Copies of all UCSF theses, dissertations, and manuscripts will be routed to the library via the Graduate Division. The library will make all theses, dissertations, and manuscripts accessible to the public and will preserve these to the best of their abilities, in perpetuity.

Please sign the following statement:

I hereby grant permission to the Graduate Division of the University of California, San Francisco to release copies of my thesis, dissertation, or manuscript to the Campus Library to provide access and preservation, in whole or in part, in perpetuity.

Russell Tolbert

Author Signature

Jan. 2, 2014

Date